Micro-engineered heart tissues on-chip with heterotypic cell composition display self-organization and improved cardiac function

Cofino-Fabres, C.; Boonen, T.; Rivera-Arbelaez, J.M.; Rijpkema, M.; Blauw, L.; Rensen, P.C.N.; ... ; Passier, R.

ADVANCED HEALTHCARE MATERIALS
www.advhealthmat.de

Micro-Engineered Heart Tissues On-Chip with Heterotypic Cell Composition Display Self-Organization and Improved Cardiac Function

*Carla Cofiño-Fabres, Tom Boonen, José M. Rivera-Arbeláez, Minke Rijpkema, Lisanne Blauw, Patrick C. N. Rensen, Verena Schwach, Marcelo C. Ribeiro, and Robert Passier**

Advanced in vitro models that recapitulate the structural organization and function of the human heart are highly needed for accurate disease modeling, more predictable drug screening, and safety pharmacology.
Conventional 3D Engineered Heart Tissues (EHTs) lack heterotypic cell complexity and culture under flow, whereas microfluidic Heart-on-Chip (HoC) models in general lack the 3D configuration and accurate contractile readouts. In this study, an innovative and user-friendly HoC model is developed to overcome these limitations, by culturing human pluripotent stem cell (hPSC)-derived cardiomyocytes (CMs), endothelial (ECs)- and smooth muscle cells (SMCs), together with human cardiac fibroblasts (FBs), underflow, leading to self-organized miniaturized micro-EHTs (μEHTs) with a CM-EC interface reminiscent of the physiological capillary lining. μEHTs cultured under flow display enhanced contractile performance and conduction velocity. In addition, the presence of the EC layer altered drug responses in μEHT contraction. This observation suggests a potential barrier-like function of ECs, which may affect the availability of drugs to the CMs. These cardiac models with increased physiological complexity, will pave the way to screen for therapeutic targets and predict drug efficacy.

1. Introduction

Cardiovascular diseases are the leading cause of death worldwide. Traditional drug discovery pipelines, mainly relying on animal models, might not be sufficiently predictive of toxic or (in)effective compounds for the human body.[1] Predictive and accurate human models are necessary to study and identify new targets for cardiac (patho-)physiologies and to screen for drug cardiotoxicity.[2]

Human pluripotent stem cells (hPSCs) can be efficiently differentiated toward cardiomyocytes (CMs)[3] and other cellular subtypes of the human heart, such as fibroblasts (FBs),[4] endothelial cells (ECs)[5] and smooth muscle cells (SMCs),[6] making them a suitable source for high-throughput applicability in drug discovery and disease modeling in vitro.[7,8] However, the heart is a complex 3D organ composed of multiple cell types with the primary function to

C. Cofiño-Fabres, J. M. Rivera-Arbeláez, V. Schwach, M. C. Ribeiro, R. Passier
Department of Applied Stem Cell Technologies
TechMed Centre
University of Twente
Enschede 7522 NB, The Netherlands
E-mail: robert.passier@utwente.nl

T. Boonen, L. Blauw, M. C. Ribeiro
River BioMedics B.V
Enschede 7522 NB, The Netherlands

J. M. Rivera-Arbeláez
BIOS Lab-on-a-Chip Group
MESA+ Institute for Nanotechnology
Max Planck Institute for Complex Fluid Dynamics
University of Twente
Enschede 7522 NB, The Netherlands

M. Rijpkema, L. Blauw, P. C. N. Rensen
Department of Medicine
Division of Endocrinology, and Einthoven Laboratory for Experimental Vascular Medicine
Leiden University Medical Center
Leiden 2300 RC, The Netherlands

R. Passier
Department of Anatomy and Embryology
Leiden University Medical Centre
Leiden 2300 RC, The Netherlands

The ORCID identification number(s) for the author(s) of this article can be found under https://doi.org/10.1002/adhm.202303664

DOI: 10.1002/adhm.202303664

pump blood to the other organs. Evidently, single cells or 2D monolayers do not fully recapitulate the complexity of the human heart. Recent studies have demonstrated the compelling feasibility of 3D cardiac organoids derived from hPSCs, that are partially reminiscent of the developing human heart, based on structure, micro-environment, and developmental processes.[9–13] Although these organoids do hold utility in developmental studies, their application in disease modeling and drug discovery is currently rather limited for several reasons. The organoids exhibit an inconsistent composition and developmental stage, along with varying quantities and distribution of cardiac cell-types within each organoid. Such substantial variability hampers their suitability as a robust basis for assay development. More importantly, these organoids lack the most pertinent cardiac readouts, including contraction force and relaxation tension as they cannot be consistently anchored to any form of force transducer. Obtaining precise measurements of these parameters in absolute units is imperative for an accurate representation of functional output in prevalent cardiac pathologies, such as heart failure.

On the other hand, 3D cardiac models, such as engineered heart tissues (EHTs), have been shown to facilitate the precise evaluation of absolute contraction force and relaxation, and have proven instrumental in the development and analysis of personalized models for cardiac diseases.[14] EHT platforms utilize supportive flexible pillars, where CMs are wrapped around to form a tissue, exerting a mechanical strain on the cardiac tissue, thereby promoting maturation, based on their structural, functional, electrophysiological and metabolic properties.[14–16] Functional parameters can be measured by tracking the displacement of these pillars.[17] However, the existing platforms for EHTs primarily require a large number of cells to generate the tissue[14,18,19] and lack the crucial element of fluid flow[20,21] (Table S1, Supporting Information). Fluid flow is essential to mimic the physiological perfusion observed in the human heart. Some Heart-on-Chip (HoC) models have attempted to address this limitation by designing customized cellular microenvironments with precise fluidic, mechanical and structural control.[22,23] However, most of these HoCs models lack the crucial 3D tissue aspect and the pillar-based technology needed for functional evaluation of cardiac tissues.[24,25] Therefore, there is a need to develop an in vitro 3D cardiac model that incorporates pillars, enabling the measurement of relevant cardiac readouts while being exposed to fluid flow. This model would replicate the nutrient and oxygen supply, removal of waste metabolites and CO_2, and drug delivery mechanisms observed in the heart.

Furthermore, in vivo, it is not the CMs, but the ECs that are exposed directly to flow, creating a functional separation between the CMs and the soluble factors present in the blood. This interaction plays a pivotal role in protection of CMs against fluidic shear stress and facilitating the uptake of fatty acids into these cells. CMs in the heart rely on fatty acids as the primary source of more than 60% of their energy supply.[26] However, CMs alone possess limited capacity to uptake a substantial amount of fatty acids, leading to an immature metabolism in hPSC-CMs. To ensure efficient uptake of fatty acids, specific proteins such as GPIHBP1 and CD36, which are predominantly expressed in ECs, are necessary.[26–31] Therefore, it is imperative to have an endothelial layer in direct contact with CMs to promote the further maturation of hPSC-CMs and accurately mimic the in vivo environment.

To replicate the vascular interface,[32,33] HoC models typically use ECs that are physically separated from the CMs by a porous membrane or by predefined microchannels composed of a biocompatible material.[34–36] These models fail to establish the essential direct physical cell-to-cell interaction, which plays a critical role in fatty acid uptake, cellular communication, self-organization, and tissue morphogenesis.[37–41] Similarly, HoC models featuring perfusable vascular networks are based on spheroid cultures.[42,43] While they facilitate the direct cell-cell crosstalk, they lack the mechanical load provided by the EHT system, thus limiting functional readouts (Table S2, Supporting Information).

Therefore, the field of cardiovascular disease calls for the development of human cardiac models capable of providing contraction force and relaxation readouts (EHTs) while cultured in a microfluidic set-up, and exhibiting a cellular composition and organization that closely resemble the in vivo conditions. This advancement holds the potential to pave the way for more accurate and clinically relevant cardiac disease modeling and drug screening.

In the current study, we addressed the challenges described above by generating a novel HoC model consisting of a microfluidic chip with four cell culture chambers which contain micropillars, resulting in the formation of functional micro-EHTs (μEHTs). Notably, we demonstrated that introduction of flow is beneficial to improve the contractile force of the μEHTs. Furthermore, incorporation of the most abundant cardiac cell types, CMs, FBs and ECs, and SMCs as supporting cells for the ECs, in these μEHTs, significantly improved cardiac functionality. Importantly, when subjected to fluid flow, the ECs exhibited a remarkable spatial self-organization within the cardiac tissue. For the first time, a dense EC monolayer around the CMs in the cardiac tissue was formed, effectively separating them from the surrounding medium and flow. The benefit of this EC barrier was observed by a delayed drug response on the contraction of the μEHTs. This highlights the relevance of ECs in these 3D cardiac models for accurate study of disease and toxicity as well as for better prediction of drug responses.

2. Results

2.1. Development of a Heart-On-Chip Platform

To achieve functional 3D cardiac tissues under fluidic flow, we designed and constructed a microfluidic HoC system comprising fluidic chambers containing flexible micropillars, enabling the formation of 3D cardiac tissues within a fluidic path. However, as the fluidic chamber is closed on all four sides, cell seeding can only be accomplished through the chip's fluidic inlet. Consequently, the 3D cardiac tissue would become attached to both the inlet and the pillars, leading to significant alterations in tissue arrangement and force distribution. This would result in highly variable outputs during contraction and relaxation. To address this challenge, we engineered a novel microfluidic HoC design featuring microfluidic burst valves positioned at the entrance and exit of each chamber. These valves effectively confine the localization of the cell suspension exclusively to the interior of the chambers (**Figure 1A,B**). Given that the production of hPSC-derived cardiac cells remains laborious and time-consuming, we minia-

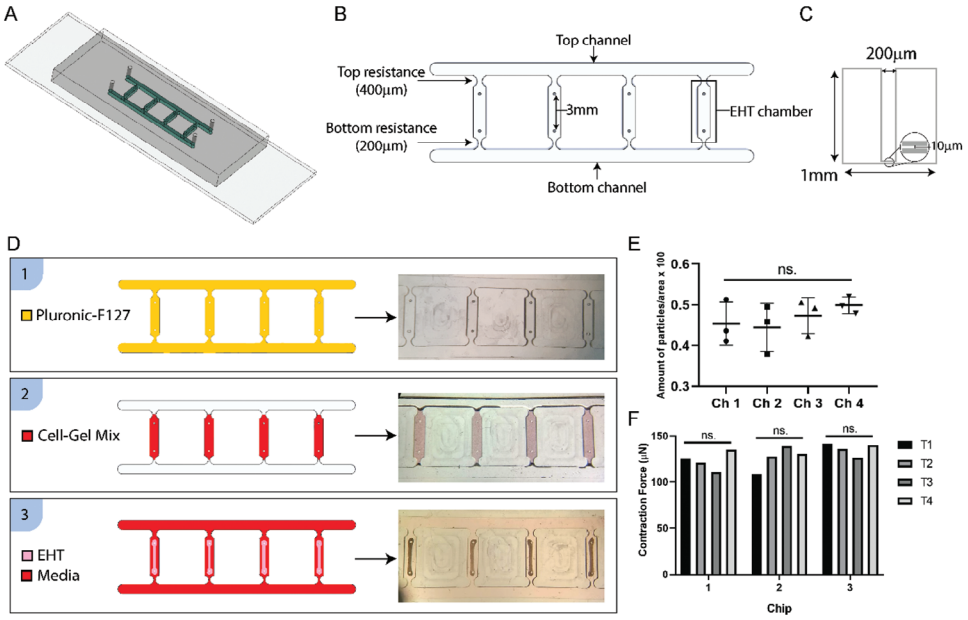

Figure 1. HoC model for µEHT generation. A) Top rendered view of the HoC bonded onto glass. B) Top view representation of the chip. Four EHT chambers of 6 mm long and 1 mm wide are flanked by a top and bottom resistance (400 and 200 µm, respectively). Each chamber contains two PDMS pillars separated by 3 mm. C) Side view representation of the chip depicting the width and length of the pillar (200 µm and 1 mm, respectively). D) Seeding procedure. First, the chip is coated with Pluronic-F127 for 20 min (1). After its removal, the cell-gel mixture is loaded and left only in the EHT chambers (2). After 10 min of cross-linking of the gel, fresh medium is added in all channels (3). E) Bead quantification shows a homogeneous distribution in each EHT chamber ($n = 4$ chips with 3 measures per chip). F) Individual contraction forces of each µEHT (bar) per chip (1,2,3) depicting no intra-chip variability. Tissues at day 10 cultured using a rocking platform. Forces determined under 1.5 Hz electrical stimulation. ($n = 3$ chips with 4 measures (tissues) per chip). E-F: One-way ANOVA with Tukey post-hoc analysis per chip; mean ± S.E.M. Ch = chamber; T = tissue; ns = not significant.

turized the chamber size (Figure 1B,C) and introduced four parallel chambers that can be seeded simultaneously. This approach not only reduces cell numbers but also minimizes dead volume per experiment, while enabling the formation and cultivation of four replicates under identical conditions with minimal handling required (Figure 1D, Video S1, Supporting Information). Furthermore, to prevent cell adhesion to the chip walls, which could compromise the integrity of the 3D tissue, we coated the PDMS with Pluronic-F127, rendering the PDMS surface non-cell adhesive.

Importantly, when the PDMS HoC was bonded to a microscope slide, a 10 µm gap was left between the tip of the pillar and the glass slide (Figure 1C). Because of this gap and the flexible nature of the PDMS, the µEHTs were able to bend the pillars. This deflection could be measured on an inverted microscope, to gain insight into the contractile properties of the µEHTs, using software that we previously developed.[17] Calcium kinetics or electrophysiological parameters can also be measured using dye-based quantification due to the close proximity of the µEHTs with an inverted microscope. Moreover, the PDMS can be peeled off the microscope slide, easily recovering the tissues for further analysis (such as RNA sequencing).

In order to guarantee that each chamber has the same volume of medium passing through, we perfused it with medium with microspheres of 10 µm. We observed no differences in particle distribution between the different chambers, indicating that the number of beads that each chamber receives is similar and that intra-chip variability is low (Figure 1E). To further validate these results, force of contraction of tissues from one chip was compared. We hypothesized that if the µEHTs would receive different nutrients from the medium, or the cell seeding procedure would affect the distribution of cells per chamber, differences in tissue performance would be observed. In accordance with the previous experiment, all four tissues, from one chip, performed similarly (Figure 1F). Therefore, we concluded that this innovative HoC design enables the accurate formation of µEHTs with minimal intra-chip variability.

2.2. Force of Contraction in µEHTs is Influenced by Cell Seeding Density and Culture Conditions under

Optimal tissue formation was assessed functionally and morphologically by adjusting the cell seeding density. Tissues were made by mixing human embryonic stem cell (hESC)-derived CMs and human adult cardiac-FBs as supporting cells. The ratio of CM:FB for µEHT formation was 10:1, based on previous findings.[44] Cells were mixed at different seeding concentrations (5.6×10^3, 11.2×10^3, or 22.3×10^3 cells μL^{-1}), which resulted in 25×10^3 (25 K), 50×10^3 (50 K), or 100×10^3 (100 K) cells per tissue, respectively. The tissues were followed over a time course of 15 days, measuring their contraction force and kinetics at day 6, 10, and 15 (**Figure** 2A). One day after seeding, compacted tissues formed and anchored to the two flexible pillars (Figure S1C, Supporting Information). Spontaneous beating was observed after 3–4 days in all tissue densities. Tissue thickness increased upon increasing cell density and remained stable within the same condition after day 10, except tissues with the lowest cell number, which broke after day 10 (Figure 2B,C). In addition, cell num-

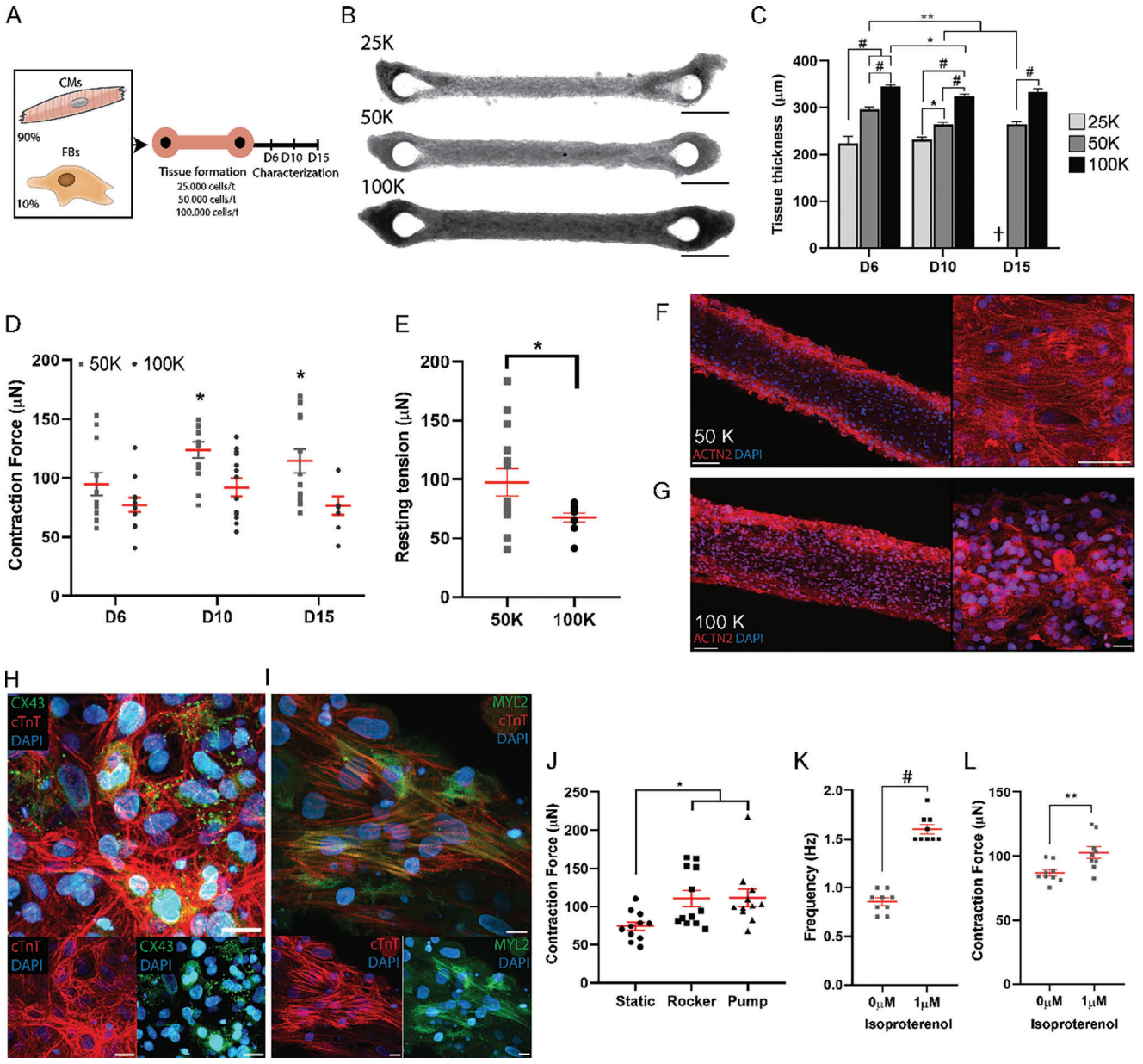

Figure 2. Force of contraction is influenced by cell seeding density and non-static culture conditions in µEHTs. A) Schematic overview of the set-up. The µEHTs are made with 90% of lactate-purified hESC-cardiomyocytes (CMs) and 10% of human adult cardiac fibroblasts (FBs) with different cell densities (t = tissue). µEHTs are monitored for fifteen days after their formation. B) Bright field image of µEHTs seeded with 25×10^3 (25 K), 50×10^3 (50 K) or 100×10^3 (100 K) cells per tissue. Scale = 500 µm. C) Thickness of µEHTs seeded with 25, 50, or 100 K cells per tissue at day 6 (D6), day 10 (D10) and day 15 (D15) (n = 6–14 tissues) † = tissues broken. D) Force of contraction measurements at day 6 (D6), 10 (D10), and 15 (D15) of tissue formation. µEHTs were electrically paced at 1.5 Hz during measurement. Note 25 K µEHTs are not shown due to rupture. Data available in Figure S1 (Supporting Information). Higher force of contraction was achieved with 50K cells per tissue at day 10 and 15 (n = 10–14 tissues, from 3 batches). E) Resting tension of the 50 and 100 K µEHTs at day 15, from figure D (n = 10–14 tissues, from 3 batches). F,G) Representative alpha-actinin (ACTN2) immunostaining of 50 (F) and 100 K (G) µEHTs at day 15 of culture. Differences were observed in ACTN2 distribution between the two seeding conditions. Scale bars: 100 (left), 10 (F right), and 20 µm (G right). H) Representative cardiac troponin T (cTnT) and connexin-43 (CX43) immunostaining of 50K µEHTs at day 15 of formation. Scale bar = 50 µm. I) Representative fluorescent image of cardiac troponin T (cTnT) and myosin light chain 2 (MYL2) in 50K µEHTs. Scale bar = 10 µm. J) Force of contraction at day 15 of 50 K µEHTs cultured in static, in a rocker platform, or in a pump system with 75 µL h^{-1} flow rate. Tissues were electrically paced at 1.5 Hz (n = 11–12 tissues, from 4 batches). K) Frequency of un-paced tissues in response to 1 µM isoproterenol in 50K tissues. Frequency increased upon addition of the drug compared to control (0 µM). L) Contraction force of tissues treated with 0 or 1 µM isoproterenol in 50 K µEHTs. Tissues were electrically paced at 2 Hz. In all experiments, except 2J (static and pump), µEHTs were cultured on a rocker platform. C,D: Two-way ANOVA; E, J: One-way ANOVA with Tukey post-hoc analysis; K-L: unpaired t-test analysis (n = 9 tissues, from 4 CM batches). Data presented as means ± SEM. *$p < 0.05$, **$p < 0.01$, #$p < 0.0001$.

ber per tissue also affected contraction performance under electrically paced conditions. A lower cell number (25 K) translated to significantly lower contraction forces at all time points analyzed (Figure S1D, Supporting Information). Surprisingly, best contraction forces were achieved when the cell number per tissue was intermediate (50 K), as shown by a significant increase of contraction force at day 10, which remained stable at day 15, when compared to lower (25 K) and higher (100 K) numbers (Figure 2D; Figure S1D, Supporting Information). More specifically, the higher contraction forces in the intermediate group also corresponded to an elevated resting tension generated by these tissues when compared to tissues seeded with the higher cell density (Figure 2E; Figure S1E, Supporting Information). Similarly, myofibrils in 100 K cells tissues appeared to be more rounded in the inside of the tissue while better myofibril distribution and stretching was observed when tissues were made with 50 K cells (Figure 2F,G). On the other hand, tissues generated with lower seeding densities (25 K) were too thin to maintain their integrity for more than 10 days. For that reason, the follow-up experiments were performed with the optimized amount of 50 K cells per μEHT. Further morphological analysis with confocal microscopy on the optimized density tissues revealed expression of maturation markers such as Connexin-43 (Cx43) and Myosin light chain 2 (MYL2) (Figure 2H,I).

To investigate whether the incorporation of more physiological dynamics would enhance the output of the 3D cardiac tissue, we compared the effect of fluid flow within the chip. Interestingly, contractile performance was improved when tissues were cultured under flow, either in a rocking system (36% increase) or connected to a pump (37% increase) when compared to static conditions (Figure 2J), highlighting the need for flow as a better representation of in vivo conditions. Of note, the fluid flow applied to the culture chamber exerts a minimal shear stress on the tissue, being approximately at least 10^4 times less than the shear stress the ECs experience in vivo.[45] Finally, we assessed the tissue response to inotropic agent isoproterenol (β-adrenergic stimulation) to assess the suitability of the chip for drug testing. As expected, tissues responded by increasing both the frequency of spontaneous beating (Figure 2K) and by exerting a higher contraction force (Figure 2L, 18% increase).

2.3. Specific Cardiomyocyte to Non-Cardiomyocyte Cell Composition and Cell Ratio is Essential for Cardiomyocyte Function and Self-Organization

2.3.1. Optimization of EC Culture in 3D

Non-CM cell-types have demonstrated a significant impact in vitro to effectively drive maturation of early fetal CMs during heart development,[37] but also to support and ensure proper cardiac function of the heart. In particular, ECs have been shown to play an essential role in maintaining heart function, while mural cells (pericytes and SMCs) are fundamental for EC organization and stability.[46,47] Hence, to mimic non-CM interactions in our HoC model we incorporated hPSC-derived ECs and SMCs. In our HoC model, the CMs are cultured in an optimized serum-free cardiac medium to enhance their performance.[16,48] However, non-CMs are commonly cultured in cell type-specific commercial media containing serum, or in basic maintenance media, such as the differentiation media (BPEL, used for generating the different cell types.[4,49,50] In light of this, our first objective was on establishing optimal culture conditions for the maintenance and growth of non-CMs (FBs, ECs, and SMCs) in our defined CM serum-free medium. For that, we cultured FBs, ECs, and SMCs only with our medium supplemented with fibroblast growth factor (FGF) and vascular endothelial growth factor (VEGF) and tested ECs' angiogenic potential and integrity in 3D fibrin gels for a period of seven days in culture (Figure S2I, Supporting Information). Consistent with previous findings,[47] ECs cultured alone connected with each other, but did not form tube-like structures, the network formed was thin and poor in integrity. When FBs or SMCs were added to ECs in a ratio of 1:2.5 or 1:5, respectively, branched and robust networks formed. When both FBs and SMCs were cultured with ECs, the resultant networks were more structured and stable over time. Moreover, both FBs and SMCs were found in close proximity to the formed capillary-like structures (Figure S2I, Supporting Information), which is a better representation on the in vivo tissue organization.[51] Therefore, the combination of these three non-CM types was chosen for further experiments.

2.3.2. Optimization of 3D Cardiac Tissue Composition

Next, to determine the optimal multicellular composition for the formation of the 3D cardiac tissues, we generated heterotypic μEHTs composed of CMs, FBs, SMCs and ECs (hereafter called CFSE-μEHTs) with varying ratios (**Figure 3A**). In total, four ratios of CM:FB:SMC:EC were examined: 1) 25CM:19FB:9SMC:47EC, 2) 50CM:12FB:6SMC:32EC, 3) 60CM:10FB:5SMC:25EC, and 4) 70CM:7FB:4SMC:19EC (referred to as 25/75, 50/50, 60/40 or 70/30 (CM:non-CM), respectively) (See Experimental Section, **Table 1**). Based on morphological analysis (Figure 3B), we found that the ratio of CMs is crucial for their continuous connectivity throughout the tissue, as lower CM:non-CM ratios (25/75 and 50/50) resulted in clusters of CMs isolated by non-CM cells. Ratios of 60/40 and 70/30 resulted in proper CM connectivity, characterized by continuous sarcomeric structures throughout the μEHT and, as expected, in higher contraction forces (Figure 3C).

However, at the highest CM ratio (70/30), the EC representation was poor, as observed by discontinuous islands of VE-Cadherin positive cells (Figure 3D). Similar to the EC representation at higher CM ratios, the presence of FBs also decreased with increasing CM contribution (Figure S3A, Supporting Information). As previously observed in fibrin gels, FBs and SMCs colocalized with the ECs (Figure 3E; Figure S3B, Supporting Information). Interestingly, in addition to the presence of FBs in close proximity to ECs, they also appeared to establish connections with clusters of ECs (Figure 3E). Connexin 43 (Cx-43) was also expressed across the various cell types, indicating potential interconnections between CMs and FBs, ECs and FBs, and CMs with CMs (Figure 3F; Figure S3C,D, Supporting Information). Immunohistochemical analysis of control CF-μEHTs further revealed possible Cx-43 mediated connec-

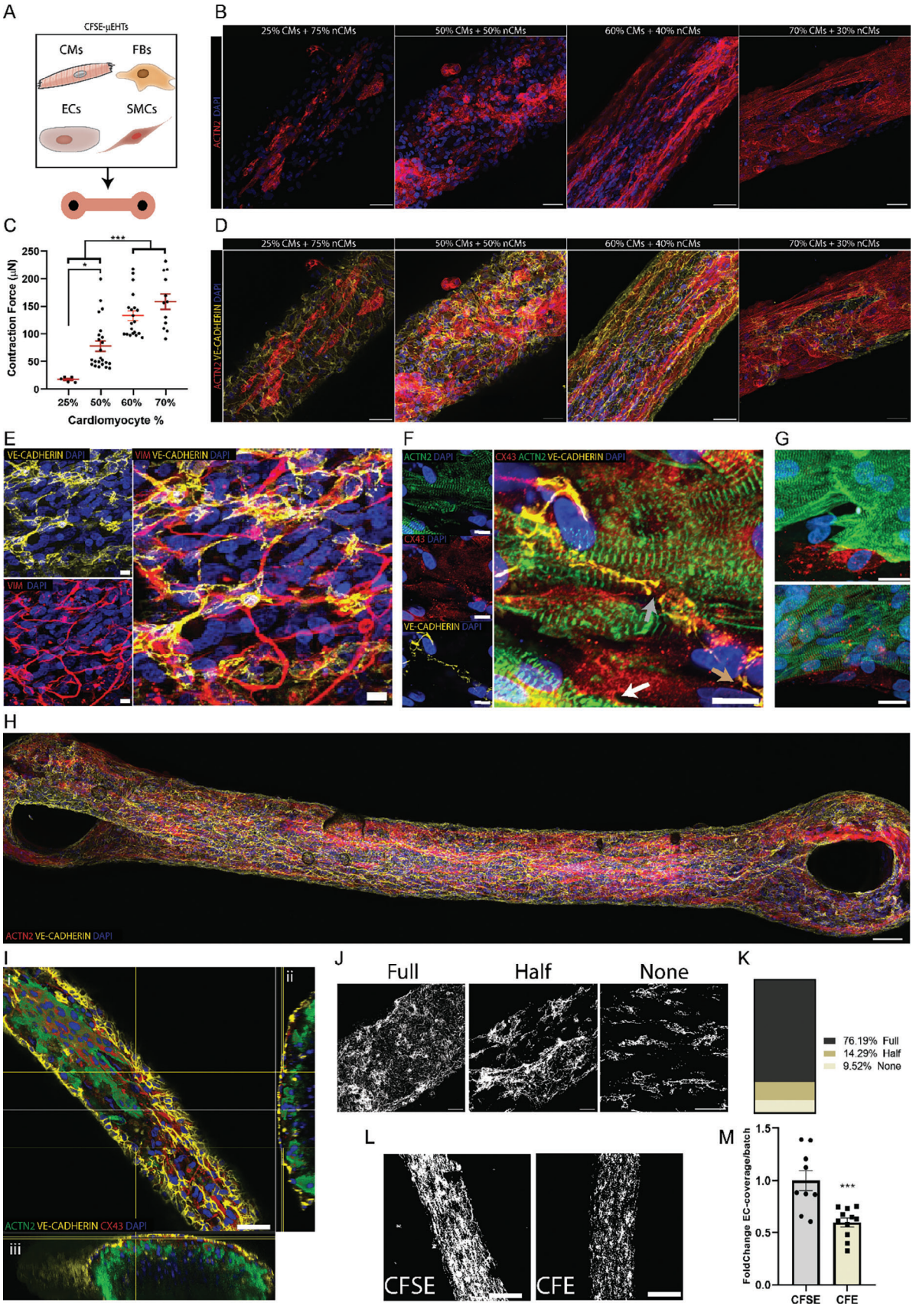

Table 1. Percentage of cells used for cell ratio optimization.

Ratio CM:nCM	%CM	%FB	%SMC	%EC
25/75	25	19	9	47
50/50	50	12	6	32
60/40	60	10	5	25
70/30	70	7	4	19

tions between CMs and FBs (Figure 3G; Figure S3E, Supporting Information).

2.3.3. ECs Self-Organize around the 3D Cardiac Tissue Underflow

Remarkably, in ratios of 60/40 and below, the majority of ECs exhibited a striking self-organization in the µEHT, forming a continuous and enveloping monolayer around the cardiac tissue under the influence of fluid flow conditions, thus closely resembling an in vivo-like EC-CM interface (Figure 3H,I; and Video S2, Supporting Information). Moreover, ECs formed networks in close contact with CMs throughout the tissues (Figure 3F; Figure S3F,G, Supporting Information). Complete EC coverage was consistently observed with a success rate of 76% (Figure 3J,K). This was successfully replicated when using and alternative hiPSC-EC line (Figure S3H, Supporting Information). Due to the role of the SMCs in maintaining EC integrity, we investigated their effect in the heterotypic µEHTs, which were formed with a ratio of 60/40 CM:non-CM. We quantified the coverage of the EC layer formed around the tissue in the presence or absence of SMCs. Notably, the absence of SMC resulted in a significant decrease in EC coverage, confirming their role in EC stability (Figure 3L,M). Next, we assessed the potential barrier-like function of the EC layer by measuring its permeability when exposed to Dextran 40 kDa. Interestingly, CFSE-µEHTs exhibited a lower permeability compared to CF-µEHTs (Figure S3I,J, Supporting Information), providing further confirmation of the shielding effect exerted by the EC layer on the tissue. Therefore, the optimal ratio of 60/40 CM to non-CM distribution was chosen for further characterization as it retained both CM connectivity and function as well as non-CM self-organization and distribution, which is consistent with what is observed in vivo.[52]

2.4. Transcriptomic Analysis Reveals Molecular Crosstalk between CMs and ECs in CFSE µEHTs

To assess the effect of the ECs and SMCs on the culture on a transcriptomic level, we performed bulk RNA sequencing of CFSE-µEHTs and compared them to µEHTs consisting of only CMs and FBs (CF-µEHTs) (**Figure 4**). Principal component analysis (PCA) and heatmaps of global gene expression illustrated a clear separation of the transcriptomes of the CF- and CFSE-µEHTs (Figure 4A; Figure S4A, Supporting Information). Differential expression analysis of CFSE- versus CF-µEHTs revealed 1164 differentially expressed genes (DEGs), of which 922 were upregulated and 242 were downregulated ($\log_2$ fold change > 0.5 and false discovery rate (FDR)-corrected $P < 0.05$, Figure 4B; and Data S1, Supporting Information). Gene ontology (GO) analysis of the up- and down-regulated genes further confirmed these observations and revealed activation of pathways associated with extracellular matrix (ECM) organization, regulation of angiogenesis and vasculogenesis, endothelium development, heart valve development, and muscle tissue development (Figure 4C). Specifically, increased expression of genes involved in ECM organization and remodeling (several metalloproteinases (*MMP2, MMP16, MMP9*), collagens (*COL12A1, COL5A1, COL1A1, COL3A1, COL1A3*) and integrins (*ITGA5*); Figure 4D; Figure S4B, Supporting Information) were observed. Moreover, cardiac endothelial-specific genes, such as ligand-receptor genes present in either the CMs or the ECs (*NOS3, EDN1, NRG1, APLN-APLNR, FSTL1-DIP2A, JAG1-NOTCH2*), EC genes involved in heart development[53] (*ENG, RAMP2, ANKRD1*, and *DCHS1*) and endocardial genes (*NPR3, HAPLN1, PLVAP, SPRX, FHL1*, and *HEY2*) were upregulated in CFSE-µEHTs (Figure 4E; Figure S4C,D, Supporting Information). Expression of genes involved in adherent and tight junction formation (*CDH5, CLDN5, PTPRB, TJP1/2*, and *ESAM*) were also upregulated in CFSE-µEHTs (Figure S4E, Supporting Information), supporting the possible role of the ECs in forming a tightly connected layer of cells around the tissue. Moreover, SMC marker genes (*ACTA2, TALGN*) and EC-SMC crosstalk-related genes (*S1PR1-TIMP2, ANGPT1-TEK*, and *EFNB2*) were also differentially expressed in CFSE-µEHTs (Figure S4F, Supporting Information). Interestingly, changes in the expression of genes associated with metabolic processes were observed, such

Figure 3. Specific cardiomyocyte to non-cardiomyocyte cell ratio is essential for cardiomyocyte function and tissue self-organization. A) Schematic overview of the set-up with CFSE-µEHTs, containing hESC-CMs, human adult cardiac FBs, hESC-cardiac SMCs and hiPSC-ECs in different ratios. Readouts are obtained ten days after tissue formation. B) Representative confocal images of µEHTs made with different percentages of CMs and non-CMs (nCMs) depicting CM organization throughout the tissue, as shown in red (ACTN2). C) Force of contraction of µEHTs made with different percentages of CMs-nCMs. One-way ANOVA with Tukey post-hoc analysis ($n = 6$–23 tissues, from 3 batches). D) Representative confocal images of µEHTs made with different percentages of CMs:nCMs showing EC (yellow, VE-cadherin) organization throughout the tissue. B and C, scale bar = 50 µm. E) Representative vimentin (red, VIM) and VE-cadherin (yellow) immunostaining of a middle section of a CFSE-µEHT made with 60% CMs+40% nCMs. Scale bar = 10 µm. F) Representative alpha-actinin (green, ACTN2), VE-cadherin (yellow) and connexin-43 (red, CX43) immunostaining of a 60% CMs+40% nCMs CFSE-µEHT. White arrow indicates a possible CM-FB interaction; Grey arrow indicates EC-expressing Cx43; Brown arrow indicates possible FB-EC interaction. Scale bar = 10 µm. G) Representative alpha-actinin (green, ACTN2) and connexin-43 (red, CX43) immunostaining of two CF-µEHTs (top and bottom). Scale bar = 10 µm. H) Representative confocal image of a full CFSE-µEHT made of 60% CMs+40% nCMs. ECs (yellow) forming a covering layer around the CMs (cTnT, red). Scale bar = 100 µm. I) Representative orthogonal confocal image of a CFSE-µEHT made of 60% CMs+40% nCMs showing CMs (red, ACTN2) and ECs (yellow, VE-cadherin). Images displaying xyz (i), xy(ii) and yz cross sectional perspectives (iii). Scale bar (for i, ii and iii) = 50 µm. J) Representative masks of VE-cadherin stained CFSE-µEHT used to quantify EC coverage around the EHTs. Full, Half, None refer to the degree of coverage. Scale bar = 20 µm. K) Quantification of EC coverage around the tissue based on the VE-cadherin masks from 21 CFSE-µEHTs as indicated in G. L) Representative masks of VE-cadherin stained µEHTs used to quantify the EC coverage in CFSE and CFE µEHTs. Scale bar = 50 µm. M) Quantification of EC-coverage in CFE- compared to CFSE-µEHTs. Data normalized per batch of tissues. Unpaired t-test ($n = 9$–11 tissues, from 3 batches). See also Figures S2 and S3 (Supporting Information). All tissues were cultured using a rocking platform. Data are presented as mean ± SEM. $*p < 0.05$, $***p < 0.005$.

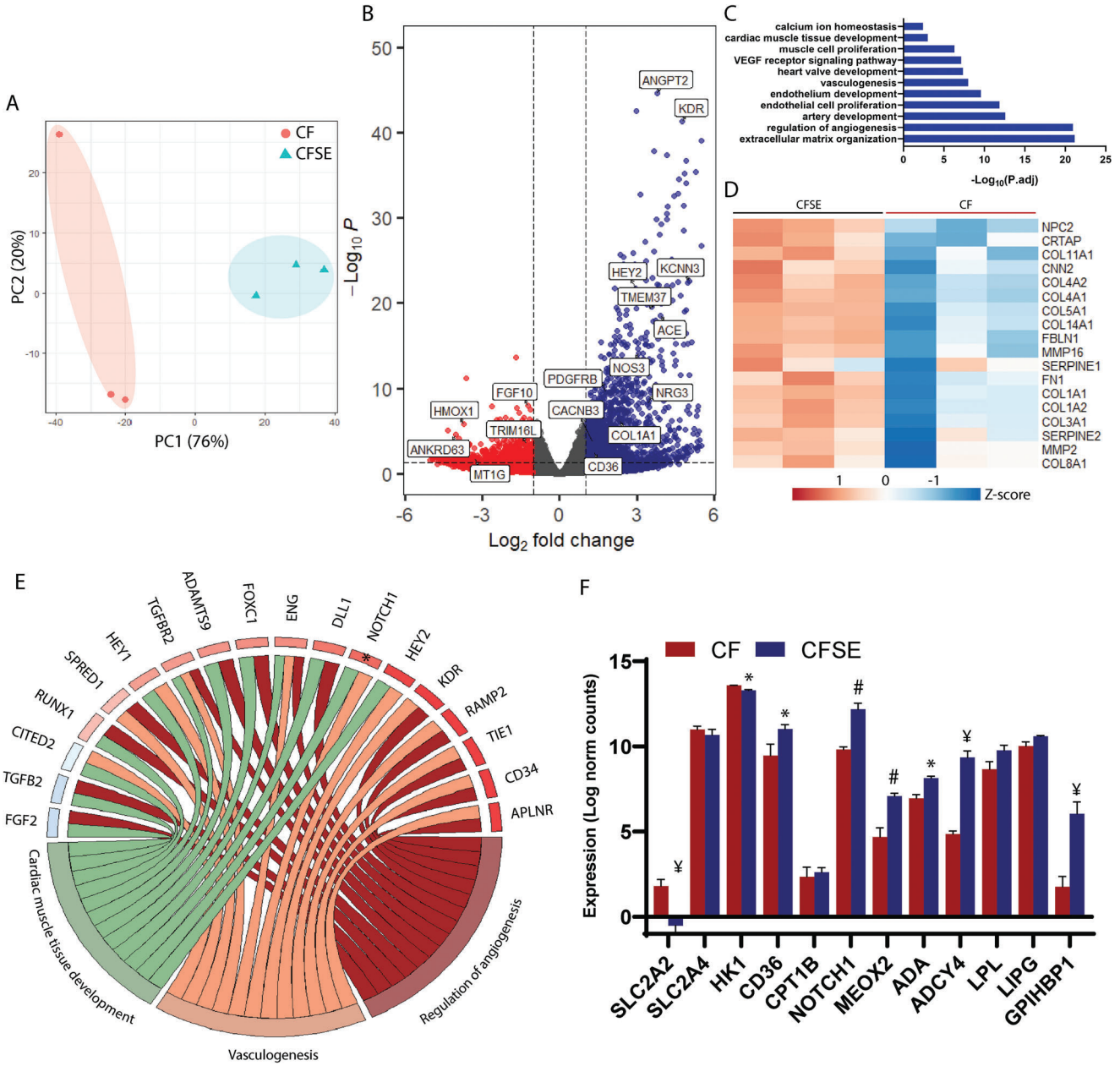

Figure 4. Transcriptional profile of CF- and CFSE-μEHTs. A) PCA plot of the two conditions (CF- and CFSE-μEHTs). B) Volcano plot representation of the up (blue, log2 fold change (LFC) > 1) and down (red, LFC <1) regulated genes in CFSE- compared to CF-μEHTs (false discovery rate (FDR) <0.05). C) GO terms upregulated in CFSE-μEHTs versus CF. D) Summarized heatmap representation of ECM-related genes based on the GO term "Extracellular matrix organization". E) GO-chord representation of three GO terms upregulated CFSE-μEHTs, showing the connection of genes from different GO categories. F) Expression values from selected genes in CF- and CFSE-μEHTs (Means ± SD, One-way ANOVA with Tukey post-hoc analysis, * $p < 0.05$; # $p < 0.01$; ¥ $p < 0.001$). See also Figure S4 (Supporting Information).

as downregulation of the glucose transporters *SLC2A2* (GLUT2) and *SLC2A4* (GLUT4) and hexokinase 1 (*HK1*) as well as upregulation of fatty acid related genes (such as *CD36, CPT1B, CPT2, ACADVL*, and *ACAT1*), suggesting that additional cell types in the μEHTs promoted a switch toward a *β*-oxidative metabolism (Figure 4F; Figure S4G, Supporting Information). Importantly, one of the most essential pathways of crosstalk between CMs and ECs regarding fatty acid uptake and transport involves the expression of *LPL* by CMs as well as expression of *GPIHBP1, CD36*, and *LIPG* by the ECs,[26–28] which were all increased in CFSE-μEHTs (Figure 4F). Of note, the presence of ECs and SMCs did not change the expression levels of cardiac sarcomeric or calcium-handling genes (Figure S4H,I, Supporting Information).

2.5. Presence of SMCs and ECs Improves Contractile Performance of µEHTs

We next compared the structural and functional performance of CF- and CFSE-µEHTs (**Figure 5**; Figure S5A and Videos S3 and S4, Supporting Information). Immunostaining for alpha-actinin 2 revealed a higher sarcomere length in CFSE-µEHTs compared to CF-µEHTs (Figure S5B, Supporting Information). Spontaneous beating frequency was similar in both tissue conditions (Figure 5A). Interestingly, although force of contraction generated at tissue level remained unaltered in the presence of ECs and SMCs (Figure 5B,C), the force normalized to the input number of CMs from CFSE-µEHTs was significantly higher than that of CF-µEHTs (Figure 5D). Strikingly, the fact that the number of CMs in CFSE-µEHTs is 16% lower than the number in CF-µEHTs, emphasizes that the normalized force is a more reliable indicator of the tissue performance, since individual CMs in the CFSE-µEHTs generate more force on average than those in the CF condition. No significant differences were observed in contraction and relaxation velocities between µEHT conditions (Figure 5E,F). Contraction and relaxation times were higher in CFSE-µEHTs (Figure S5C,D, Supporting Information). The increase in contraction and relaxation times might be explained by an increased contraction force, as the tissue needs to exert more force to bend the pillars. However, comparing velocities with times may not be straightforward, since velocities consider the entire contraction and relaxation duration while times are calculated at specific percentages (10 and 90%). Furthermore, the additional cell types allowed CMs to better maintain synchronized contraction transients in response to higher stimulation frequencies (4 and 5 Hz), thus exhibiting a higher maximum capture rate (Figure 5G,H). This might suggest that the inclusion of these cell types facilitates a rapid transmission of the electrical signal through the tissue, indicative of a higher conductivity. In agreement, post-rest potentiation (PRP), a measure of the capacity of the sarcoplasmic reticulum (SR) in CMs to store, efficiently release and subsequently replenish Ca^{2+}, also showed a significant force increase in the presence of ECs and SMCs (enhancement of force by 62 ± 7% in CFSE-µEHTs vs 15 ± 5% in CF) (Figure 5I,J). Taken together, our results suggest that adding multiple cell types in the µEHTs results in better functional performance.

2.6. Presence of SMCs and ECs Improves Electrophysiologic Aspects of µEHTs

Electrical properties of the tissues in CF or CFSE conditions were also examined, with the membrane potential dye FluoVolt. Representative traces and activation maps of normalized fluorescence intensity of one action potential (**Figure 6**A,B) revealed a prolonged action potential duration at 90% of the repolarization (APD_{90}) in CFSE- µEHTs (Figure 6C), with no disruptions in the electrical propagation throughout the tissue (Videos S5 and S6, Supporting Information). Importantly, CFSE-µEHTs exhibited an enhanced conduction velocity (Figure 6D). The observed upregulation of multiple connexins (*GJA1, GJA5*, and *GJA4*) in CFSE-µEHTs (Figure 6E), along with the expression of Cx-43 throughout the entire EC layer covering the cardiac tissue (Figure S3C,D, Supporting Information), suggest the potential involvement of ECs in augmenting the conduction velocity.

Next, we examined whether Ca^{2+} handling was enhanced in CFSE-µEHTs. Ca^{2+} transients, as determined using a Ca^{2+}-sensitive dye during pacing, revealed that the time to peak was comparable between both culture conditions. However, CFSE-µEHTs exhibited a reduced time to 80% of decay, indicating accelerated relaxation kinetics in comparison to CF-µEHTs (Figure 6F,G). These findings provide further support that the presence of multiple cell types exerts a maturation effect on the cardiac tissue.

2.7. Impact of Self-Organized Endothelial Cell Layer on Cardiomyocyte Drug Response at a Functional Level

The endothelium serves as a critical regulator of molecular transport to the cardiac muscle heart musculature, acting as a physical barrier between the blood circulation and CMs.[54] We hypothesized that, given the observed self-organization of the ECs in our µEHTs, causing a reduction of the permeability to dextran (Figure S3I,J, Supporting Information), functional responses to drugs may be influenced by the presence or absence of the endothelial layer. We found that both CF- and CFSE-µEHTs exhibited an expected dose-dependent positive and negative inotropic response to isoproterenol and verapamil, respectively (**Figure 7**A,B). However, the magnitude of tissue response to each drug was diminished in CFSE- compared to CF-µEHTs, suggesting that the CMs were most likely less exposed to the drug due to the presence of the endothelial barrier. To further investigate the potential modulatory role of ECs in drug response, CF- and CFSE-µEHTs were exposed for 24 h to a widely used clinically relevant cardiotoxic drug, doxorubicin, followed by functional assessment over time (Figure 7C,D). Interestingly, when the outer EC layer covered the 3D tissue, a delay in the force decrease was observed after treatment (significantly different at 9 h for 5 µM and at 24 h for 1 µM). Taken together, these findings indicate that the ECs may act as a separating barrier between the medium and CMs, reducing CM drug response at a functional level.

3. Discussion

In this study, we successfully developed a novel and user-friendly HoC model by introducing microfluidic burst valves, allowing for the formation and culture of µEHTs within fluidic chambers under controlled flow conditions. The addition of microfluidic burst valves in the chip design facilitated the confinement of the cell-gel mixture within individual chambers, allowing us to significantly decrease the size of the EHTs in a precise and reproducible manner. Moreover, by using this chip, time of seeding is reduced and no further tissue manipulation is needed. In contrast, conventional EHT culture systems require extensive fabrication and elaborate seeding procedures and/or involve an extra step of transfer of the newly made EHTs to another culture well, which may compromise tissue integrity.[14,21,55] While several EHT (pillar-based) platforms have demonstrated the feasibility of reducing the number of cells per tissue, required to reduce production costs and facilitate upscaling,[21,56,57] to date, only two

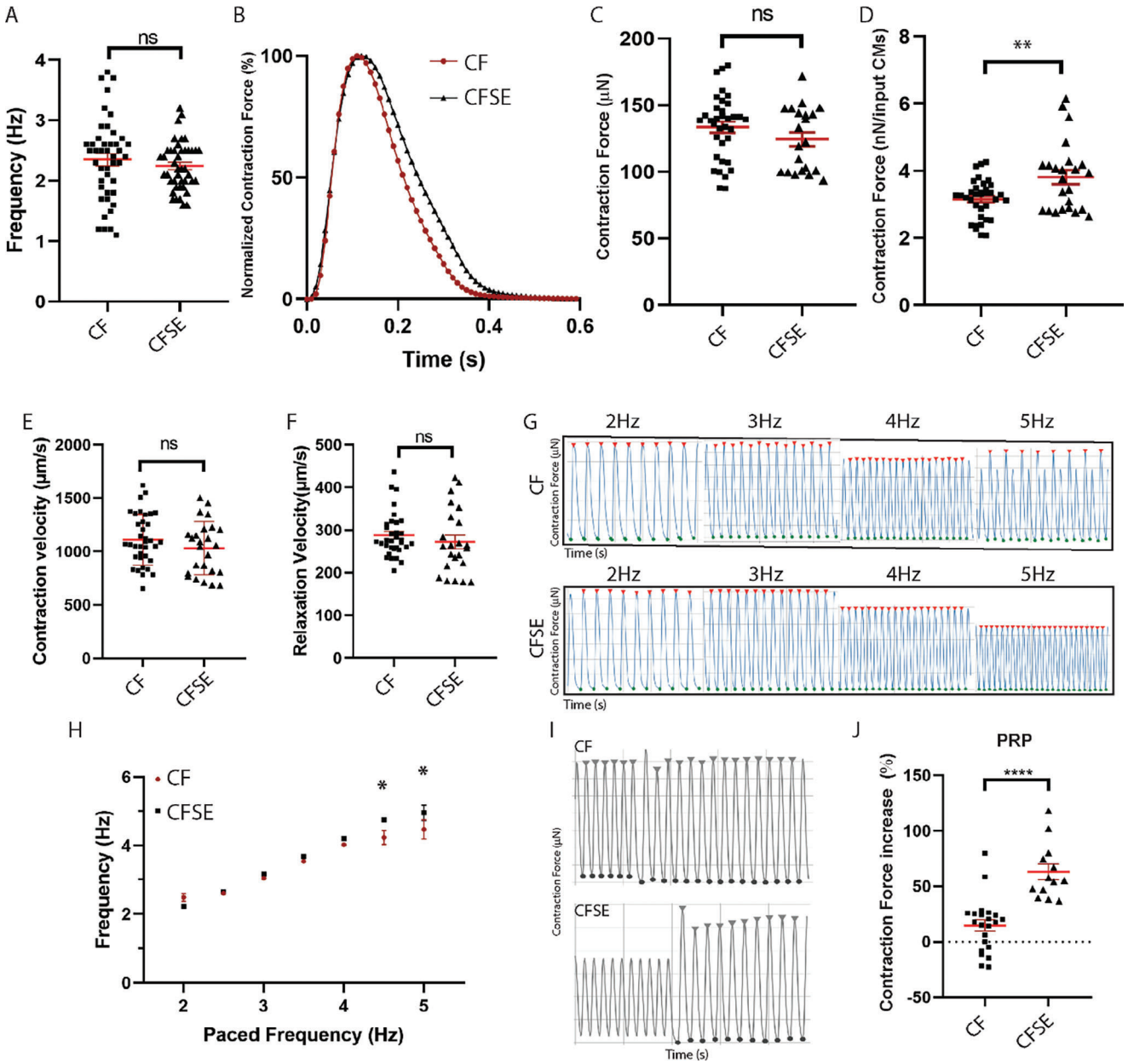

Figure 5. Addition of SMCs and ECs improves the functional properties of the µEHTs. A) Frequency of contraction in CF- and CFSE-µEHTs (n = 24–35 tissues/condition, from 3 batches). B) Representative plot of force over time in CF- and CFSE-µEHTs. C) Contraction force CF- and CFSE-µEHTs (n = 24–35 tissues/condition, from 3 batches). D) Contraction force normalized by the total number of seeded CMs in CF- and CFSE-µEHTs (n = 24–35 tissues/condition, from 3 batches). E,F) Contraction (E) and relaxation (F) velocity in CF- and CFSE-µEHTs (n = 24–35 tissues/condition, from 3 batches). G) Representative trace of contraction forces in CF- (top) and CFSE- (bottom) µEHTs being paced with increasing stimulation frequency. Note CF tissues stop following the pacing after 4 Hz. H) Maximum capture rate: Frequency of CF- (red) and CFSE- (black) µEHTs paced at increasing stimulation frequencies. Two-way ANOVA (n = 16-18 tissues/condition, from 3 batches). I) Representative traces of post-rest potentiation (PRP) in CF- (top) and CFSE- (bottom) µEHTs. Note first peak after high frequency pacing (>5 Hz). J) Post-rest potentiation (PRP) of CF- and CFSE- µEHTs depicting the percentage of force increase after high intensity pacing (height of the first peak after high intensity pacing normalized to the first peak height) (n = 13–22 tissues/condition, from 3 batches). All tissues were cultured under a rocking platform. B–E: tissues paced at 1.5 Hz during measurement. Data analyzed with unpaired t-test and presented as means ± S.E.M. unless otherwise stated. Ns = not significant, *$p < 0.05$, **$p < 0.01$,****$p < 0.0001$. See also Figure S5 (Supporting Information).

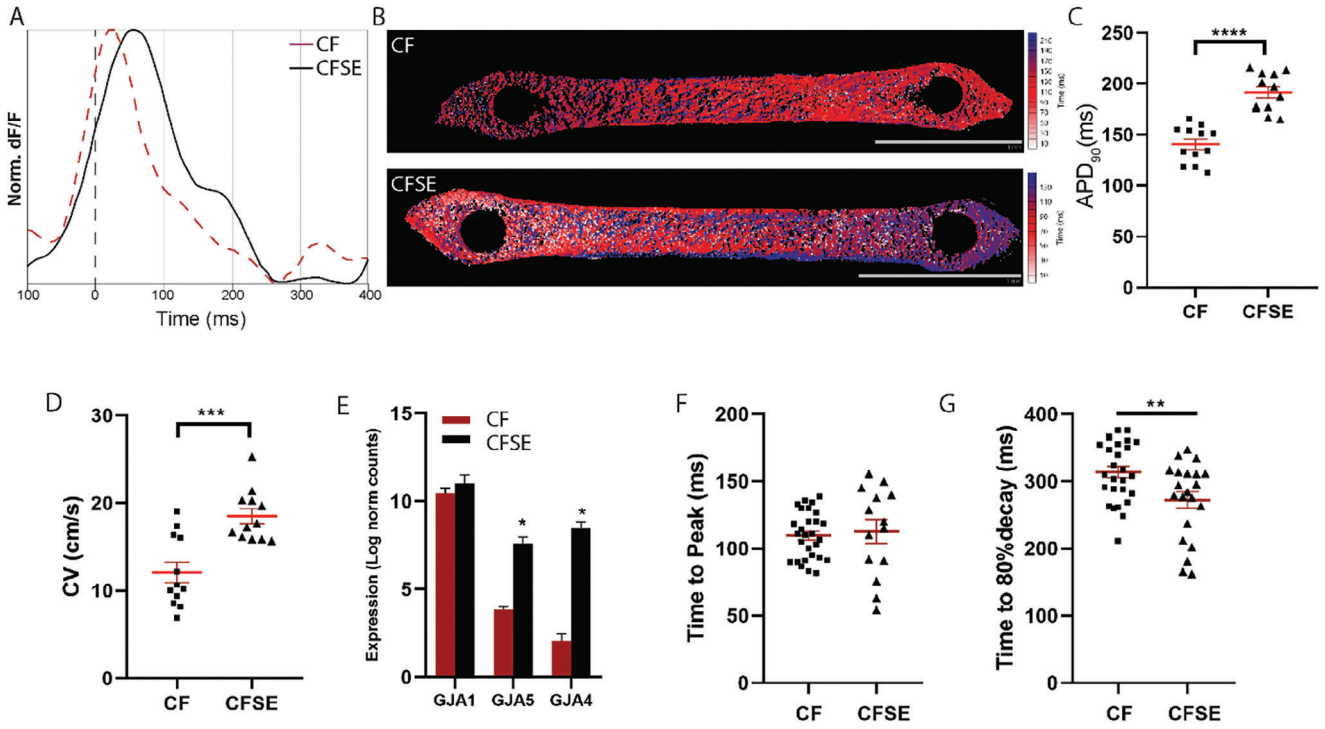

Figure 6. Electrical performance in CF- and CFSE-μEHTs. A) Representative changes in the fluorescence intensity of the FluoVolt-AP indicator over time in CF- (red) and CFSE- (black) μEHTs. B) Representative activation maps of CF- (top) and CFSE- (bottom) μEHTs. C) Action potential duration at 90% (APD90) repolarization in CF- and CFSE-μEHTs stimulated at 2 Hz (unpaired t-test; $n = 12$ tissues/condition, from 3 batches). D) Conduction velocity of CF- and CFSE-μEHTs stimulated at 2 Hz (unpaired t-test; $n = 12$ tissues/condition, from 3 batches). E) Expression values of connexin coding genes in CF- and CFSE-μEHTs from bulk RNA sequencing. One-way ANOVA with Tukey post-hoc analysis ($n = 3$ batches). F,G) Calcium transient parameters (Time to peak (F) and Decay time at 80% (G) of CF- and CFSE-μEHTs stimulated at 2 Hz (unpaired t-test; $n = 20$–25 tissues/condition, from 3 batches). All tissues were cultured under a rocking platform. Data are presented as means ± SEM. *$p < 0.05$, **$p < 0.01$, ****$p < 0.0001$.

microfluidic EHT (pillar-based) platforms have been described (Table S1, Supporting Information).[58,59] Nevertheless, the heterotypic formation and comprehensive characterization of EHTs under flow have not been previously described. Our work describes that the culture of μEHTs under dynamic flow conditions results in a significant improvement in contractile performance, highlighting the importance of incorporating flow in creating realistic in vitro cardiac 3D models. Additionally, contractility readouts in our HoC can be easily extracted using software that we have previously developed[17] to infer on CM's performance. Also, since the μEHTs in the HoC are always positioned at the same height on the pillars because of the hanging configuration, variation in contraction readouts is greatly reduced. Importantly, the critical assessment of contractile forces is unattainable in current developmental-based organoid models due to their inability to anchor to force transducers,[10,60] making 3D EHTs much better models to mimic cardiomyopathies, such as heart failure. Moreover, the tissues are in close proximity to the glass slide, facilitating the integration of the functionality with live cell imaging to evaluate calcium kinetics and electrophysiological parameters.

After conducting the initial characterization of μEHTs consisting of CMs and FBs to optimize the μEHT culture conditions, we identified a threshold at which increasing the number of cells to the culture chamber size did not yield an increase of contraction force. As previously reported, tissue thickness can affect nutrient and oxygen diffusion through the tissue,[61] however, this may not be the only contributing factor to the decrease in functional performance of larger tissues. Instead, we found an inverse relationship between the resting tension on the pillars and the number of cells forming the tissue. Resting tension is defined as diastolic preload exerted by the pillars on the tissue. Since in our HoC model, preload is not dependent on varying pillar distances, changes in the resting tension could be explained by the cell number. When the number of cells of formed μEHTs are too low, tissues cannot sustain the tension over multiple days and therefore break. In contrast, a low tension, as seen in the highest cell number condition, did not result in an anisotropic alignment of the cells, but instead the CMs displayed a spherical-like morphology, which consequently led to lower generated resting and contraction forces. Therefore, the effect of an intermediate number of cells per tissue most likely provided more space to the CMs to spread through the tissue's matrix, resulting in better CM organization and stretching. This most likely increased the resting tension and consequently, the contraction force. This is in accordance with studies showing that higher isotropy induces lower contraction forces[62] and that an increase of preload (variation of stretch) up to a certain degree, enhances contraction force, measured under isometric conditions.[63] Our findings highlight the importance of titrating the number of cells for optimal cardiac anisotropy and force generation.

While external factors such as flow and tension (preload) play a significant role in the performance of the cardiac tissue, the

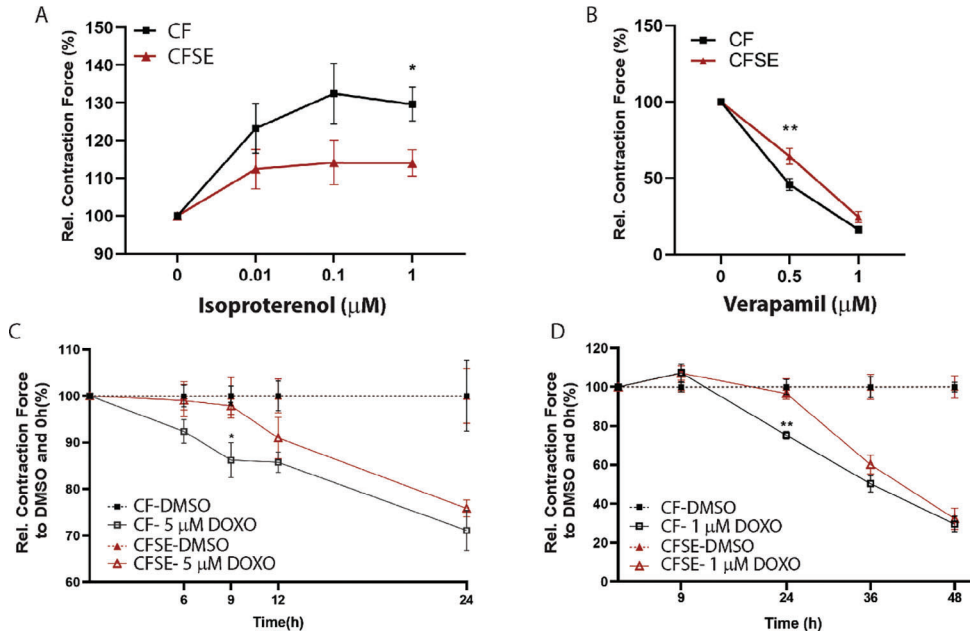

Figure 7. Functional performance to drugs is influenced by addition of cell types in CFSE-μEHTs. A) Contraction force increase in response to increasing doses (0 to 1 μM) of isoproterenol administration normalized to initial force in CF- and CFSE-μEHTs (n = 12 tissues/condition, from 3 batches). B) Contraction force in response to increasing concentrations of verapamil (0 to 1 μM) normalized to initial force in CF- and CFSE-μEHTs (n = 9 tissues/condition, from 3 batches). Asterisk in A,B indicate significant difference between CF and CFSE treated at the indicated drug concentration. C,D) Normalized contraction force in CF- and CFSE-μEHTs treated with doxorubicin (DOXO) (C, 5 μM for 24 h or D, 1 μM for 48 h). Asterisks indicate significant difference between CF and CFSE treated with DOXO (n = 12 tissues/condition, from 3 batches). All tissues were cultured under a rocking platform. Tissues paced at 2 Hz during measurement. Data analyzed with Two-way ANOVA and presented as means ± SEM. ns = not significant, *$p < 0.05$, **$p < 0.01$.

cellular composition is equally crucial for accurately replicating the in vivo environment of the heart. Therefore, we believe that incorporating multiple factors together provides the best opportunities to create the most representative in vitro models. Due to the essential role of ECs in maintaining heart's homeostasis and supplying CMs with free fatty acids,[26,41] and the evidence that EC signaling improves CM maturation (Table S2, Supporting Information),[4,64] we introduced hiPSC-derived ECs, in combination with hESC-derived cardiac SMCs, to the existing hESC-CMs and human adult cardiac FBs in our μEHTs. However, one of the main challenges is to culture and maintain cells in a common medium that is suitable for all cell types.[65,66] We have previously established a serum-free cardiomyocyte medium to avoid serum-induced effects on cell morphology, signaling, batch-to-batch variability, and altered drug responses, while enhancing CM performance.[16,48] Here we have successfully adjusted this serum-free medium by adding factors that were also favorable for FB and EC cultures.

In line with previous work, the addition of multiple cell types in our μEHTs improved the overall tissue performance (Table S2, Supporting Information). We extensively characterized the effect of the EC and SMC addition in the μEHTs by performing transcriptomic, morphological, and functional analyses. We demonstrate that structurally, culturing with ECs and SMCs resulted in an improved sarcomeric length, similar effects observed in other studies (Table S2, Supporting Information).[4,67,68] Functionally, the benefit of an heterotypic composition was reflected by an enhanced contraction force, post-rest potentiation, and maximum capture rate, as well as by an improved electrophysiology (increased conduction velocity and longer APD90) and calcium relaxation kinetics (shortened calcium time to decay). Some of these individual enhancements align with previously reported studies (Table S2, Supporting Information).[4,43,49,64,67–74] However, it is important to note that most of these studies have been performed in other culture systems, such as spheroids or cell sheets, which facilitate the evaluation of electrophysiological parameters but lack the mechanical load and quantification of contraction forces. On the other hand, previous studies utilizing EHTs to evaluate the impact of EC addition have predominantly focused solely on contraction force readouts. Therefore, a significant advantage of our study lies in the comprehensive characterization of the effect of heterotypic cell composition on the μEHTs through comprehensive molecular, histological, and functional analyses. On a gene expression level, we observed an enhanced expression of genes encoding for ECM proteins, reported to play a role in CM maturation,[64] and cAMP, which has been shown to play a role in CM maturation and assembly of Cx-43 gap junctions.[4] The expression of nitric oxide synthase (*NOS3*), genes associated with cAMP signaling (*ADCY4, ADCY5*, and *GUCY1A2*), and various genes encoding for gap junctions was higher in CFSE-μEHTs, which supports the notion that ECs regulate CM contractility by releasing nitric oxide and prostacyclin, thereby influencing the myocardial cAMP/cGMP ratio.[38,41] Conversely, expression levels of calcium-related genes, such as *RYR2* and *CACNA1C*, and genes encoding for sarcomeric proteins did not change. Further characterization through single-cell RNA se-

quencing would be beneficial to distinguish the effect of EC and SMC addition on gene expression within each cell type, since differences in CM number between both µEHT conditions might currently obscure these effects.

Notably, through careful adjustment of the CMs to non-CMs ratio, we observed that ECs exhibited a robust self-organization process, forming a dense layer surrounding the cardiac tissue under flow conditions. This spontaneous organization was observed consistently across various batches of EC differentiation and different hiPSC-EC lines. This engineered-based self-organization in 3D cardiac tissues differs from endocardial, myocardial, and epicardial layers in spherical cardioid-like cultures[9] or 3D spheroid-like bioprinted structures,[75] where there is limited control over the identity, developmental stage and distribution of cells in the tissue. In addition, it has been demonstrated that flow can induce polarization of ECs, resulting in the formation of a single cell layer with the apical side exposed to the blood flow.[76] Hence, the introduction of flow in our HoC model may have triggered ECs to organize in the outer layer of the µEHTs that directly interfaces with perfused flow, which suggests the importance of flow for cellular self-assembly in 3D tissues.

Next to the maturation-inducing effects exerted by non-CMs to CMs, the endothelial layer in vivo plays a pivotal role as a barrier for nutrient and drug transport to the adjacent CMs within the heart.[77,78] Direct interaction of CMs and ECs is particularly important for the uptake of fatty acids, which account for over 60% of the energy source in adult cardiomyocytes.[79] CMs themselves are incapable of adequately capturing free fatty acids from the medium or blood due to the absence or lower expression of key fatty acid transporting proteins such as GPIHBP1[27,28] and CD36, which are mainly expressed by ECs that separate the cardiomyocytes from the blood.[26] Direct interaction of CMs and ECs promotes LPL transport from the CMs to the interstitial space, from where its translocated to the capillary lumen of the ECs.[80] Therefore, the lack of interaction between ECs and CMs is considered a major factor contributing to the metabolic immaturity of hPSC-CMs. In this study we demonstrate for the first time the formation of a polarized, self-organized heterotypic EHT, exhibiting enhanced expression of genes associated with fatty acid uptake. The formation of an endothelial outer layer formation may offer the advantage of establishing a CM-EC interface without physical impeding the contraction of the CM tissue. Current EHT or HoC models that include ECs, either disrupt CM continuity through a vascular bed without perfusion,[49,81] which was recently shown to reduce contractile performance,[42] or are organized in perfusable channels, separated by a membrane that prevents direct EC-CM contact.[35] Hence, our presented model provides a more physiological relevant EC-CM interphase compared to what has been previously described.

An important advantage of the self-organized CFSE-µEHTs in the microfluidic device is that it enables studying drug responses under flow conditions in the presence of an outer layer of ECs that are wrapped around the CMs, more accurately recapitulating the uptake of drugs via ECs toward CMs, as it occurs in vivo. Interestingly, we observed a delayed functional response to inotropic modulators and the cardiotoxic drug doxorubicin in µEHTs with an outer EC layer. While further research is needed to fully elucidate the precise mechanism behind this effect, our findings suggest a potential role of the EC layer in modulating drug responses.

4. Conclusion

In summary, we successfully developed an innovative HoC model that enables for the first time the polarized formation of 3D heterotypic human cardiac tissues under flow conditions, composed of four key cardiac cell types, and their functional assessment. This yielded significant improvements in contraction force and electrophysiological parameters of the engineered 3D cardiac tissues. Importantly, it also enabled the formation of a distinct endothelial outer layer, establishing an active EC-CM crosstalk that contributed to enhanced cardiac tissue performance, shielding the cardiac tissue from fluid shear and acting as a barrier to compound uptake, evident in the delayed responses to pharmacological agents. This model represents a significant advancement in the field of in vitro cardiac models, laying the foundation for the development of more representative and personalized cardiac disease models in the future.

5. Experimental Section

HPSC Culture: The experiments were performed using the human embryonic stem cell (hESC) lines NKX2.5$^{EGFP/+}$-COUP-TFII$^{mCherry/+}$[82] and NKX2.5$^{EGFP/+}$-ACTN2$^{-mRubyII/+}$[83] and the human induced pluripotent stem cell (hiPSC) lines LU54 (LUMC0054iCTRL#2) and WTC-11 (WT GM25256*G0002 or mEGFP-TJP1 tagged, AICS-0023). HiPSCs and hESCs were maintained as undifferentiated colonies in Essential 8 medium (Thermo Fisher, A1517001) on vitronectin (Thermo Fisher, A31804)-coated 6-well plates (Greiner Bio-One, 657 160). HiPSCs were passaged with 0.5X Revitacell (Thermo Fisher, A2644501).

Differentiation of hPSCs to CMs: Differentiation of hESCs to CMs was performed as previously described.[48] Briefly, one day before starting the differentiation, hESCs were seeded at a density of 20–25 × 10^3 cells per cm^2 on Matrigel (83 µg protein mL^{-1}) (Corning, 354 230)-coated 6-well plates in Essential 8 medium. After 24 h (day 0), mesodermal differentiation was induced by addition of Activin-A (20 – 30 ng mL^{-1}, Miltenyi 130–115-010), BMP4 (20 – 30 ng mL^{-1}, R&D systems 314-BP/CF) and WNT activator CHIR99021 (1.5 – 2.25 µmol L^{-1}, Axon Medchem 1386) in BPEL medium.[84] At day 3, BPEL containing WNT inhibitor XAV939 (5 µmol L^{-1}, R&D Systems 3748) was used to refresh cells. On days 7 and 10, cells were refreshed with plain BPEL. Beating CMs at day 13 were metabolically selected with a lactate purification step of 4 days. Lactate purification medium consisted of the previously described cardiomyocyte medium[48] without glucose and with an additional 5 mM of sodium DL-lactate solution (60%, Sigma Aldrich, L4263). At day 17, purified CMs were kept for three more days in cardiomyocyte medium consisting of the above described lactate purification medium with additional 4.5 mM of D(+)-Glucose (Millipore, 1 083 371 000). Afterward, cells were dissociated with Triple 10X (ThermoFisher, A1217702) and cryopreserved in freezing medium comprising 50% Knockout serum replacement (KOSR) (ThermoFisher, 10 828 028), 40% cardiomyocyte medium, 10% DMSO (Sigma-Aldrich, D2650), and 0.5% RevitaCell. Cells with at least 90% of green fluorescent protein signal (GFP, representing NKX2.5-positive cardiomyocytes) were used for downstream applications (Figure S1A,B, Supporting Information).

Differentiation of hPSCs into Cardiac Smooth Muscle Cells: NKX2.5$^{EGFP/+}$-ACTN2-$^{mRubyII/+}$ hESC were differentiated to cardiac smooth muscle cells (SMCs) with an adapted protocol from[85] (Figure S2, Supporting Information). One day prior the start of the differentiation, hPSC were seeded at a density of 20 × 10^3 cells per cm^2 on Matrigel (83 µg protein mL^{-1})-coated 6-well plates in Essential 8 medium. After 24 h (day 0; D0), mesodermal differentiation was induced by the addition of Activin-A (20 ng mL^{-1}), BMP4 (20 ng mL^{-1}), and WNT activator CHIR99021 (1.5 µM) in BPEL medium. At day 3 (D3) and day 6 (D6) cells were refreshed with BPEL containing all-trans retinoic acid (RA, Sigma Aldrich, R2625) (1 µM) and BMP4 (30 ng mL^{-1}) to induce cardiac

specification to the epicardial lineage. On day 9 (D9), pro-epicardial cells were passaged to fibronectin (2 µg mL^{-1}) (Sigma, F1141)-coated T175 flasks at a density of 26 × 10^3 cells per cm^2 in BPEL medium containing TGFβ inhibitor SB431542 (Tocris Bioscience, 1614/10) (10 µM). Induction toward smooth muscle cells was induced by refreshing the medium to BPEL plus TGFβ1 (PeproTech, 100–21) (5 ng mL^{-1}) and bFGF-2 (Miltenyi Biotec, 130-093-564) (10 ng mL^{-1}) on day 10 (D10) and day 12 (D12). Afterward, cells were maintained in full SmGM-2 medium (Lonza, CC-3182) until day 20, when they were cryopreserved at passage number 1 in CryoStor CS10 (StemCell Technologies, 0 7930). For characterization studies, SMCs were thawed and seeded in fibronectin (2 µg mL^{-1}) -coated 6 or 96 wells plates and maintained in SmGM-2 medium until cells reached 80% confluency (Figure S2A, Supporting Information).

Differentiation of Endothelial Cells: LUMC0054iCTRL#2 hiPSCs were differentiated to ECs as described previously [5] with minor modifications. Briefly, mesoderm induction was initiated at day 0 by refreshing with BPEL medium supplemented with CHIR99021 (8 µM). At day 3, 6, and 9 cells were refreshed with vascular specification medium consisting of VEGF (50 ng mL^{-1}) (Miltenyi Biotec, 130-109-384) and SB431542 (10 µM) in BPEL. HiPSC-ECs were isolated on day 10 using CD31-Dynabeads (Thermo Fisher Scientific), as previously described.[5] Afterward, isolated hiPSC-ECs were expanded for 3–4 days in Human Endothelial-serum free medium (EC-SFM) (Thermo Fisher, 11 111 044) supplemented with 1% human platelet-poor serum (Biomedical Technologies, BT-214), VEGF (30 ng mL^{-1}) and bFGF-2 (20 ng mL^{-1}) (Miltenyi Biotec, 130-093-564) and cryopreserved at passage number 1 in CryoStor CS10.

Cardiac Fibroblast Expansion: Human adult cardiac fibroblasts (FBs) were purchased from Promocell (C-12375) and expanded according to their protocol.[86] Briefly, a T175 cell culture flask (Greiner) was incubated (at 37 °C and 5% CO_2) with 12 mL of FGM-3 (Promocell, C-23130) for 30 min. After thawing at 37 °C, the cells were transferred from the cryovial to a cell culture flask containing the FGM-3 with an additional 18 mL of FGM-3. Whenever the cells reached a 70–90% confluency in the flask, the cells were passaged; this process was repeated until reaching 11 passages. Then, FBs were frozen at a final concentration of 150 × 10^3 cells 0.5 mL^{-1} in freezing medium. The freezing medium consists of 50% KOSR, 40% FGM-3, 10% DMSO, and 0.5% Revitacell.

Design and Fabrication of the HoC: A design for the positive mold of the HoC was made using SolidWorks (Dassault Systèmes). Consecutively, this design was produced using a Computer Numerical Control (CNC) micro-milling machine (Datron Neo, Datron AG) from a polymethyl methacrylate (PMMA) block. Polydimethylsiloxane (PDMS) (Sylgard 184 Silicone elastomer kit, Dow corning, USA) was cast onto the positive mold and cured in an oven at 65 °C for >4 h. After curing, the PDMS was removed from the mold, in- and outlets were punched using a 1 mm biopsy punch (Robbins Instruments, USA) and the individual chips were cut out. Each chip was exposed to air plasma (50 W) for 40 s (Cute, Femto Science, South Korea) and bonded onto a glass PDMS spin-coated glass slide (1 mL PDMS, 1,500 rpm, 30 s, 1000 rpm s^{-1} (Spin150, Polos, The Netherlands)).

Particle Quantification: To assess the intra-chip variability, chips were loaded with cardiomyocyte medium loaded with 1:25 10 µm beads (Polysciences, 17 136) and placed in the incubator at 37 °C, 5% CO_2 for 10 min. After that, each chamber of the chip was imaged. Beads per chamber were quantified using particle analyzer from Fiji Software, Image J.

Generation and Culture of Micro-EHTs: HoCs were coated with 1% Pluronic F-127 (P2443-250G, Sigma) in DPBS for 20 min at room temperature (RT), after which, they were dried using an aspiration system.

Preparation of Cell Suspensions for Seeding Density Optimization Experiments: hPSC-CMs and FBs were thawed, centrifuged at 240 g for 3 min, resuspended in cardiomyocyte medium supplemented with bFGF-2 (5 ng mL^{-1}) and counted. Afterward, CM and FB cell suspensions were mixed in a ratio of 90:10 with the different seeding concentrations: 5.6 × 10^3, 11.2 × 10^3, and 22,3 × 10^3 cells µL^{-1}. The resulting cells per tissue were: 25 × 10^3, 50 × 10^3, and 100 × 10^3, respectively. The HoC model was further characterized using the 11.2 × 10^3 cells µL^{-1} seeding density (50 × 10^3 cells per tissue).

Preparation of Cell Suspension for CFSE Cell Ratio Optimization Experiments: For CFSE-µEHTs, three to four days prior the seeding, hiPSC-ECs (P1) were thawed and cultured on 1% gelatin-coated plates in EC-SFM plus 1% Human platelet poor serum, VEGF (30 ng mL^{-1}) and bFGF-2 (20 ng mL^{-1}) and refreshed two days after thawing. Afterward, cells were dissociated with TryplE 1X (Thermo Fisher, 12 563 029) for 3 min at 37 °C, 5% CO_2, centrifuged for 3 min at 300 g, resuspended in cardiomyocyte medium supplemented with VEGF (50 ng mL^{-1}) and bFGF-2 (5 ng mL^{-1}) (hereafter called full cardiomyocyte medium) and counted. CMs, FBs, and SMCs were thawed, centrifuged at 240 g for 3 min, resuspended in full cardiomyocyte medium, and counted. Then, CM, FB, SMC, EC (CFSE) cell suspensions were mixed in four different ratios (Table 1): 1) 25:19:9:47, 2) 50:12:6:32, 3) 60:10:5:25, or 4) 70:7:4:19 (referred to as 25/75, 50/50, 60/40, or 70/30 (cardiomyocyte to non-cardiomyocyte, CM:nCM, respectively) in a final concentration of 13.2 × 10^3 cells µL^{-1} (59 × 10^3 cells per tissue). To compare the effect of EC and SMC addition on the tissues, CF-µEHTs, consisting of CMs and FBs in a 90:10 ratio were mixed to a concentration of 10.5 × 10^3 cells µL^{-1} (47 × 10^3 cells per tissue) and compared to CFSE-µEHTs generated with the 60:40 ratio (CM:nCM).

Cell Seeding into the Chip: For each condition, the appropriate number of cells were pooled and centrifuged. Per HoC, 60 µL of gel-cell mixture was made by mixing 10% of Fibrinogen (2 mg mL^{-1} final concentration, Sigma-Aldrich F8630), 10% Matrigel (1 mg mL^{-1} final concentration), 1% aprotinin (final concentration 2.5 µg mL^{-1}, Sigma-Aldrich, A1153), and 80% of cells. Right before seeding, 0.3% thrombin (Sigma, T7513) was added to the gel-cell mixture. Immediately after adding the thrombin, the mixture was mixed and seeded into the chip by pipetting it into the top channel, after which the chambers filled until the bottom resistance (Video S1, Supporting Information). Subsequently, the mixture was removed from the top channel while the top resistance ensured that the gel-cell mixture remained in the chambers. The gel was polymerized in the chambers for 10 min at RT. The appropriate culture medium was added by placing two pipettes with 45 µL in one side and two with 190 µL in the other. µEHTs were maintained at 37 °C and 5% CO_2. 24 h after seeding, medium was refreshed. For CF- and CFSE comparison experiments, additional DAPT (StemCell Technologies, #72 082) (10 µM) was added to the medium on day 1 for 24 h. Unless stated, µEHTs were maintained at 37 °C and 5% CO_2 either in a rocker platform and refreshed every two days or in a Harvard pump with a flow rate of 75 µL h^{-1}. Rocking platform was preferred over the pump due to the easiness of handling and upscaling possibilities.

Force Measurement: Force of contraction was measured on days 6, 10, and 15 or only on day 10 after tissue formation. Briefly, bright field movies were recorded using a Nikon ECLIPSE Ti2 inverted microscope (RRID:SCR_02 1068) under temperature and humidity control (37 °C and 5% CO_2), using a high-speed camera at 100 frames per second (fps) with 3x magnification. Two platinum electrodes (Advent Research Materials) were placed in two diagonal inlets of the chip to electrically stimulate the µEHTs using a custom-made pacing device at 1.5 Hz (10 ms biphasic pulses, 3 V cm^{-1}) for 20 s. High-frequency response was assessed by recording tissue contraction from 2 to 5 Hz (0.5 Hz increase every 20 s). At 5 Hz, stimulation was kept for 1 min and turned off to measure the post-rest potentiation (PRP) of the force (values expressed in percentage of the first peak height).

Responses to drugs were assessed at day 10. First, contraction force of the tissues was measured. Second, medium from the top and bottom channel of the chip was removed and pre-warmed control medium (0 µM) was added, incubated for 10 min under temperature and humidity control (37 °C and 5% CO_2) and tissues were measured again. Then, for a positive inotropic response, isoproterenol (Sigma, I5627) was administrated at 0.01, 0.1, and 1 µM in the same manner as described above, and after 10 min of incubation, force of contraction was measured. Similarly, negative inotropic effects were determined with 0.5 and 1 µM of verapamil (Sigma, V4629). Gain or loss of force was assessed with respect to control condition (0 µM) in each case. For doxorubicin (Sigma-Aldrich, D1515) treatment, tissues' force of contraction was measured and the tissues were refreshed with 1 or 5 µM of the drug or DMSO. Force was evaluated over the course of 24–48 h. Unless stated, all contraction force measurements after drug exposure were performed with electrical stimulation at 2 Hz (10 ms biphasic pulses, 3 V cm^{-1}) for 20 s.

Force kinetics analysis was quantified by tracking and measuring the displacement of the pillars over time using a custom-made python-based software, adjusted from the previous work.[17] The contraction force of the µEHTs was assessed using the elastic beam bending Equation (1).[87]

$$F = \frac{3\pi E R^4}{2a^2\,(3L - a)}\delta \quad (1)$$

Where F is the µEHT contraction force; E, R, L represent Young's modulus, radius, and length of the PDMS pillar: a is the height of the tissue on the pillars from the base and δ is the measured distance between pillars.

In addition to force kinetics, the custom-made python-based software also calculates the resting tension, which was the force generated on the pillars by the tissue during its formation. This resting tension was calculated as the change in distance between the pillars with and without µEHTs.

Electrophysiology Characterization with Voltage-Sensitive Dye: Estimation of the action potential kinetics (APD90) and the conduction velocity was carried out by membrane potential staining of the µEHTs with the FluoVolt membrane potential kit (Thermo Fisher Scientific, cat no. F10488) according to manufacturer's instructions with minor modifications. Briefly, a fresh aliquot of FluoVolt Loading solution was prepared by mixing PowerLoad Concentrate (component B, 1:100) and FluoVolt dye (Component A, 1:1000) in HBSS (Gibco, 14 025 092). Medium was completely removed from the tissues, washed first with HBSS, and then incubated with the FluoVolt Loading solution for 1 h at 37 °C. Thereafter, tissues were washed twice with pre-warmed HBSS, stimulated at 2 Hz, and imaged in a Nikon ECLIPSE Ti2 fluorescent microscope under temperature and humidity control (37 °C and 5% CO_2) according to manufacturer instructions. Videos were analyzed with BV Workbench, Brainvision Inc.

Calcium Analysis: Tissues were loaded with Fluo-8 AM (Abcam, AB142773) (4 µM) dye in HBSS buffer for 1 h at 37 °C. Afterward, tissues were washed once with pre-warmed HBSS and left in cardiomyocyte medium for 30 min at 37 °C before recording. For recordings, µEHTs were stimulated at 2 Hz and imaged in a Nikon ECLIPSE Ti2 fluorescent microscope under temperature and humidity control (37 °C and 5% CO_2). Analysis was performed using a custom-made Matlab software.

Immunofluorescence Analysis: Whole-mount staining of µEHTs was performed as described in.[16] Briefly, µEHTs were fixed after 10–15 days of culture for 1 h at RT in 4% paraformaldehyde (PFA), washed at RT with 0.3% Triton-X 100 (Sigma-Aldrich; 3 × 20 min), blocked for non-specific binding with 3% BSA (Sigma-Aldrich, A9418), 0.3% Triton-X 100 (Sigma-Aldrich, T8787)), and 0.1% Tween20 (Merck, P9416) in PBS overnight at 4 °C. Primary antibodies were added for 2 days at 4 °C. Then, tissues were washed at RT with 0.3% Triton-X 100 (3 × 20 min), and secondary antibodies and DAPI were added overnight at 4 °C and protected from light. Next day, tissues were washed three times with PBS for 20 min each at RT. All incubations were done on a shaker. Finally, µEHTs were mounted on a microscope slide with a 0.25 mm spacer (SunJin Lab, IS216) for confocal imaging with a Zeiss LSM 880 microscope.

To determine the success rate of EC cover formation in CFSE-µEHTs, a total of 21 VE-cadherin stained tissues were first processed into a binary mask in Fiji Software (ImageJ) and classified according to three categories (full, half, or none coverage). Quantification of EC coverage in CFE- and CFSE-µEHTs was performed on VE-cadherin intensity, calculated in Fiji Software, ImageJ. Intensities of CFE-µEHTs were normalized to the those of CFSE-µEHTs and per batch of µEHTs.

Calculation of sarcomere length was performed on images captured by confocal microscope of alpha-actinin immunostaining using standard analysis in Fiji Software, ImageJ. In short, one area from one picture representing a cardiomyocyte was selected and an intensity plot was obtained. By measuring the distance between the intensity peaks, sarcomere length from one cardiomyocyte could be extrapolated. This measurement was performed in 40 areas per condition.

Permeability Assay: Permeability of the EC-layer was evaluated with Dextran-40 kDa FITC (ThermoFisher Scientific, D1845). For that, CF and CFSE-uEHTs were first stained with CD31-APC (1:10, ThermoFisher, 17-0319-42) for 20 min at RT. After two washes with HBSS, tissues were treated with blebbistatin (Sigma Aldich, B0560) (5 µM) for 30 min at 37 °C. After two washes with HBSS, the HoC was mounted on the confocal stage with the appropriate microfluidic setup to infuse the 1:1000 Dextran-40 kDa. Confocal z-stack imaging was performed in each tissue at 0, 2, 10, and 15 min after dextran infusion. The same area of the tissue was imaged. Quantification of the permeability was assessed by measuring the fluorescence difference between timepoint 0 and the following timepoints, in the orthogonal view of the tissue.

Gene Expression (Bulk-RNA Sequencing): RNA from 4 µEHTs per condition in triplicate (3 CF and 3 CFSE) at day 10 after tissue formation was isolated and purified using the Nucleo Spin RNA kit (Macherey-Nagel) according to manufacturer's instructions. RNA sequencing was performed by GenomeScan (Leiden, the Netherlands). Quality and integrity of the RNA were confirmed using a Fragment Analyzer (Agilent Technologies). Library preparation was performed using the NEBNext Ultra II Directional RNA Library Prep Kit for Illumina (New England Biolabs, E7760S/L). After complementary DNA synthesis and polymerase chain reaction enrichment, quality and yield was measured with the Fragment Analyzer and confirmed the expected size distribution (average size range, 300–500 base pairs). Clustering and DNA sequencing (with 1.1 nM of DNA) was performed with a NovaSeq6000 DNA sequencer (Illumina) according to manufacturer's protocols and using NovaSeq control software NCS v1.8. Image analysis, base calling, and quality check was performed with the Illumina data analysis pipeline RTA3.4.4 and Bcl2fastq (v2.20). Sequence reads were trimmed and filtered on low-quality bases using fastp (v0.23.2). Trimmed reads were mapped to the Homo sapiens reference genome (GRCh38.p13) using STAR2 (v2.7.10) and read counts were determined using HTSeq (v2.0.2). Differential gene expression was performed by analyzing read counts with the DESeq2 package (v2-1.36) in R (v4.2.0). Genes with absolute log2 fold change > 1.0 (>2-fold absolute change) and FDR corrected p <0.05 were considered differentially expressed and visualized with pheatmap (v1.0.12) and EnhancedVolcano package (v1.14.0). Gene ontology analysis was performed with package clusterProfiler (v4.4.4). Log-scaled normalized counts were used to compare the gene expression levels between samples.

Statistics: Statistical analysis was performed using GraphPad Prism 8. Statistical significances are indicated in each figure. One-way ANOVA, two-way ANOVA, Student's t test for paired or unpaired analysis were applied accordingly to evaluate the differences in means between groups and/or conditions. Results were displayed as mean ± SEM unless stated otherwise and were considered significantly different with p values <0.05.

Supporting Information

Supporting Information is available from the Wiley Online Library or from the author.

Acknowledgements

M.C.R. and R.P. contributed equally to this work. C.C.-F. and T.B. share first authorship. This work was supported by the TOP-ZonMw grant, (ZonMw, TOP-00812-98-17061) and Health Holland TKI-LSH (LSHM 19004). The authors thank their colleagues S.A. ten Den and K. Vermeul for providing hiPSC derived ECs.

Conflict of Interest

R.Passier is a cofounder of Pluriomics (Ncardia) and River BioMedics BV. M.C.Ribeiro and L.Blauw are cofounders of River BioMedics BV. The other authors report no conflict.

Data Availability Statement

The data that support the findings of this study are available from the corresponding author upon reasonable request.

Keywords

cardiomyocytes (CMs), endothelial cells (ECs), engineered heart tissues (EHTs), heart-on-Chip (HoC), human pluripotent stem cells (hPSC), microfluidics

Received: October 26, 2023
Revised: January 30, 2024
Published online:

[1] S. Pasteuning-Vuhman, R. de Jongh, A. Timmers, R. J. Pasterkamp, *Trends Mol Med* **2021**, *27*, 263.
[2] H. Savoji, M. Hossein, N. Rafatian, S. Ahadian, M. Radisic, *Biomaterials* **2019**, *198*, 3.
[3] M. J. Birket, M. C. Ribeiro, A. O. Verkerk, D. Ward, A. R. Leitoguinho, S. C. Den Hartogh, V. V. Orlova, H. D. Devalla, V. Schwach, M. Bellin, *Nat. Biotechnol.* **2015**, *33*, 970.
[4] E. Giacomelli, V. Meraviglia, G. Campostrini, A. Cochrane, X. Cao, R. W. J. van Helden, A. Krotenberg Garcia, M. Mircea, S. Kostidis, R. P. Davis, *Cell Stem Cell* **2020**, *26*, 862.
[5] V. V. Orlova, F. E. van Den Hil, S. Petrus-Reurer, Y. Drabsch, P. Ten Dijke, C. L. Mummery, *Nat. Protoc.* **2014**, *96*, 1514.
[6] D. Iyer, L. Gambardella, W. G. Bernard, F. Serrano, V. L. Mascetti, R. A. Pedersen, S. Sinha, A. Talasila, **2016**, *143*, 904.
[7] S. R. Braam, L. Tertoolen, A. van de Stolpe, T. Meyer, R. Passier, C. L. Mummery, *Stem Cell Res.* **2010**, *4*, 107.
[8] H. Liang, M. Matzkies, H. Schunkert, M. Tang, H. Bonnemeier, J. Hescheler, M. Reppel, *Cell. Physiol. Biochem.* **2010**, *25*, 459.
[9] P. Hofbauer, S. M. Jahnel, N. Papai, M. Giesshammer, A. Deyett, C. Schmidt, M. Penc, K. Tavernini, N. Grdseloff, C. Meledeth, *Cell* **2021**, *184*, 3299.
[10] Y. R. Lewis-Israeli, A. H. Wasserman, M. A. Gabalski, B. D. Volmert, Y. Ming, K. A. Ball, W. Yang, J. Zou, G. Ni, N. Pajares, X. Chatzistavrou, W. Li, C. Zhou, A. Aguirre, *Nat. Commun.* **2021**, *12*, 5142.
[11] G. Rossi, A. Boni, R. Guiet, M. Girgin, R. G. Kelly, M. P. Lutolf, *bioRxiv* **2019**, 802181.
[12] B. Volmert, A. Kiselev, A. Juhong, F. Wang, A. Riggs, A. Kostina, C. O'Hern, P. Muniyandi, A. Wasserman, A. Huang, Y. Lewis-Israeli, V. Panda, S. Bhattacharya, A. Lauver, S. Park, Z. Qiu, C. Zhou, A. Aguirre, *Nat. Commun.* **2023**, *14*, 8245.
[13] C. Schmidt, A. Deyett, T. Ilmer, S. Haendeler, A. Torres Caballero, M. Novatchkova, M. A. Netzer, L. Ceci Ginistrelli, E. Mancheno Juncosa, T. Bhattacharya, *Cell* **2023**, *186*, 5587.
[14] I. Mannhardt, K. Breckwoldt, D. Letuffe-Brenière, S. Schaaf, H. Schulz, C. Neuber, A. Benzin, T. Werner, A. Eder, T. Schulze, *Stem Cell Rep.* **2016**, *7*, 29.
[15] S. S. Nunes, J. W. Miklas, J. Liu, R. Aschar-Sobbi, Y. Xiao, B. Zhang, J. Jiang, S. Massé, M. Gagliardi, A. Hsieh, N. Thavandiran, M. A. Laflamme, K. Nanthakumar, G. J. Gross, P. H. Backx, G. Keller, M. Radisic, *Nat. Methods* **2013**, *10*, 781.
[16] M. C. Ribeiro, J. M. Rivera-Arbeláez, C. Cofiño-Fabres, V. Schwach, R. H. Slaats, S. A. ten Den, K. Vermeul, A. van den Berg, J. M. Pérez-Pomares, L. I. Segerink, J. A. Guadix, R. Passier, *J. Pers. Med.* **2022**, *12*, 214.
[17] J. M. Rivera-Arbeláez, C. Cofiño-Fabres, V. Schwach, T. Boonen, S. A. ten Den, K. Vermeul, A. van den Berg, L. I. Segerink, M. C. Ribeiro, R. Passier, *PLoS One* **2022**, *17*, 0266834.
[18] K. Ronaldson-Bouchard, S. P. Ma, K. Yeager, T. Chen, L. Song, D. Sirabella, K. Morikawa, D. Teles, M. Yazawa, G. Vunjak-Novakovic, *Nature* **2018**, *556*, 239.
[19] Y. Zhao, N. Rafatian, E. Y. Wang, N. T. Feric, B. F. L. Lai, E. J. Knee-Walden, P. H. Backx, M. Radisic, *Matrix Biol.* **2019**, *85*, 189.
[20] R. J. Mills, B. L. Parker, G. A. Quaife-Ryan, H. K. Voges, E. J. Needham, A. Bornot, M. Ding, H. Andersson, M. Polla, D. A. Elliott, L. Drowley, M. Clausen, A. T. Plowright, I. P. Barrett, Q.-D. Wang, D. E. James, E. R. Porrello, J. E. Hudson, *Cell Stem Cell* **2019**, *24*, 895.
[21] M. Dostani, L. M. Windt, J. M. Stein, B. J. van Meer, M. Bellin, V. Orlova, M. Mastrangeli, C. L. Mummery, P. M. Sarro, P. M. Sarro are, *J. Microelectromech. Syst.* **2020**, *29*, 881.
[22] B. Zhang, A. Korolj, B. F. L. Lai, M. Radisic, *Nat. Rev. Mater.* **2018**, *38*, 257.
[23] C. Liu, X. Feng, G. Li, P. Gokulnath, J. Xiao, *EBioMedicine* **2022**, *76*, 103813.
[24] A. Marsano, C. Conficconi, M. Lemme, P. Occhetta, E. Gaudiello, E. Votta, G. Cerino, A. Redaelli, M. Rasponi, *Lab Chip* **2016**, *16*, 599.
[25] A. Vivas, C. IJspeert, J. Y. Pan, K. Vermeul, A. van den Berg, R. Passier, S. S. Keller, A. D. van der Meer, *Adv. Mater. Technol.* **2022**, *7*, 2101355.
[26] I. J. Goldberg, R. H. Eckel, N. A. Abumrad, *J. Lipid Res.* **2009**, *50*, S86.
[27] B. S. J. Davies, A. P. Beigneux, R. H. Barnes, Y. Tu, P. Gin, M. M. Weinstein, C. Nobumori, R. Nyrén, I. Goldberg, G. Olivecrona, *Cell Metab.* **2010**, *12*, 42.
[28] A. P. Beigneux, B. S. J. Davies, P. Gin, M. M. Weinstein, E. Farber, X. Qiao, F. Peale, S. Bunting, R. L. Walzem, J. S. Wong, *Cell Metab.* **2007**, *5*, 279.
[29] G. Olivecrona, T. Olivecrona, *Curr. Opin. Lipidol.* **2010**, *21*, 409.
[30] J. S. Flier, L. H. Underhill, R. H. Eckel, *N. Engl. J. Med.* **1989**, *320*, 1060.
[31] S. antamarina-Fojo, K. A. Dugi, *Curr. Opin. Lipidol.* **1994**, *5*, 117.
[32] O. King, I. Sunyovszki, C. M. Terracciano, *Pflugers Arch. Eur. J. Physiol.* **2021**, *473*, 1117.
[33] D. Huh, B. D. Matthews, A. Mammoto, M. Montoya-Zavala, H. Y. Hsin, D. E. Ingber, *Science (80-.).* **2010**, *328*, 1662.
[34] J. U. Lind, M. Yadid, I. Perkins, B. B. O'Connor, F. Eweje, C. O. Chantre, M. A. Hemphill, H. Yuan, P. H. Campbell, J. J. Vlassak, *Lab Chip* **2017**, *17*, 3692.
[35] B. Zhang, M. Montgomery, M. D. Chamberlain, S. Ogawa, A. Korolj, A. Pahnke, L. A. Wells, S. Massé, J. Kim, L. Reis, *Nat. Mater.* **2016**, *15*, 669.
[36] B. W. Ellis, A. Acun, U. I. Can, P. Zorlutuna, *Biomicrofluidics* **2017**, *11*, 024105.
[37] G. J. Scuderi, J. Butcher, *Front Cell Dev Biol* **2017**, *5*, 50.
[38] A. Colliva, L. Braga, M. Giacca, S. Zacchigna, *J Physiol* **2020**, *598*, 2923.
[39] O. King, I. Sunyovszki, C. M. Terracciano, *Pflugers Arch.* **2021**, *473*, 1117.
[40] D. A. Narmoneva, R. Vukmirovic, M. E. Davis, R. D. Kamm, R. T. Lee, *Circulation* **2004**, *110*, 962.
[41] D. L. Brutsaert, *Physiol. Rev.* **2003**, *83*, 59.
[42] U. Arslan, M. Brescia, V. Meraviglia, D. M. Nahon, R. W. J. van Helden, J. M. Stein, F. E. van den Hil, B. J. van Meer, M. Vila Cuenca, C. L. Mummery, *Stem Cell Rep.* **2023**, *18*, 1394.
[43] O. King, D. Cruz-Moreira, A. Sayed, F. Kermani, W. Kit-Anan, I. Sunyovszki, B. X. Wang, B. Downing, J. Fourre, D. Hachim, *Cell Rep Methods* **2022**, *2*, 100280.
[44] Y. Zhao, N. Rafatian, E. Y. Wang, N. T. Feric, B. F. L. Lai, E. J. Knee-Walden, P. H. Backx, M. Radisic, *Matrix Biol.* **2020**, *85*, 189.
[45] K. H. K. Wong, J. M. Chan, R. D. Kamm, J. Tien, *Annu. Rev. Biomed. Eng.* **2012**, *14*, 205.
[46] R. K. Jain, *Nat. Med.* **2003**, *9*, 685.
[47] M. Vila Cuenca, A. Cochrane, F. E. van den Hil, A. A. F. de Vries, S. A. J. Lesnik Oberstein, C. L. Mummery, V. V. Orlova, *Stem Cell Rep.* **2021**, *16*, 2159.
[48] M. J. Birket, M. C. Ribeiro, G. Kosmidis, D. Ward, A. R. Leitoguinho, V. van de Pol, C. Dambrot, H. D. Devalla, R. P. Davis, P. G. Mastroberardino, *Cell Rep.* **2015**, *13*, 733.
[49] O. Caspi, A. Lesman, Y. Basevitch, A. Gepstein, G. Arbel, I. H. M. Habib, L. Gepstein, S. Levenberg, *Circ. Res.* **2007**, *100*, 263.

[50] L. Gao, Z. R. Gregorich, W. Zhu, S. Mattapally, Y. Oduk, X. Lou, R. Kannappan, A. V. Borovjagin, G. P. Walcott, A. E. Pollard, *Circulation* **2018**, *137*, 1712.
[51] A. N. Stratman, G. E. Davis, *Microsc. Microanal.* **2012**, *18*, 68.
[52] F. Weinberger, K. Breckwoldt, S. Pecha, A. Kelly, B. Geertz, J. Starbatty, T. Yorgan, K.-H. Cheng, K. Lessmann, T. Stolen, *Sci. Transl. Med.* **2016**, *8*, 363ra148.
[53] E. Helle, M. Ampuja, A. Dainis, L. Antola, E. Temmes, E. Tolvanen, E. Mervaala, R. Kivelä, *Front. Cell Dev. Biol.* **2021**, *9*, 2135.
[54] A. R. Pinto, A. Ilinykh, M. J. Ivey, J. T. Kuwabara, M. L. D'Antoni, R. Debuque, A. Chandran, L. Wang, K. Arora, N. A. Rosenthal, *Circ. Res.* **2016**, *118*, 400.
[55] A. Hansen, A. Eder, M. Bönstrup, M. Flato, M. Mewe, S. Schaaf, B. Aksehirlioglu, A. Schwörer, J. Uebeler, T. Eschenhagen, *Circ. Res.* **2010**, *107*, 35.
[56] T. Boudou, W. R. Legant, A. Mu, M. A. Borochin, N. Thavandiran, M. Radisic, P. W. Zandstra, J. A. Epstein, K. B. Margulies, C. S. Chen, *Tissue Eng. Part A* **2012**, *18*, 910.
[57] R. J. Mills, D. M. Titmarsh, X. Koenig, B. L. Parker, J. G. Ryall, G. A. Quaife-Ryan, H. K. Voges, M. P. Hodson, C. Ferguson, L. Drowley, *Proc. Natl. Acad. Sci. USA* **2017**, *114*, E8372.
[58] H. Parsa, B. Z. Wang, G. Vunjak-Novakovic, *Lab Chip* **2017**, *17*, 3264.
[59] N. Huebsch, B. Charrez, G. Neiman, B. Siemons, S. C. Boggess, S. Wall, V. Charwat, K. H. Jæger, D. Cleres, Å. Telle, *Nat. Biomed. Eng.* **2022**, *6*, 372.
[60] G. Rossi, N. Broguiere, M. Miyamoto, A. Boni, R. Guiet, M. Girgin, R. G. Kelly, C. Kwon, M. P. Lutolf, *Cell Stem Cell* **2021**, *28*, 230.
[61] M. Radisic, J. Malda, E. Epping, W. Geng, R. Langer, G. Vunjak-Novakovic, *Biotechnol. Bioeng.* **2006**, *93*, 332.
[62] A. C. C. Van Spreeuwel, N. A. M. Bax, A. J. Bastiaens, J. Foolen, S. Loerakker, M. Borochin, D. W. J. Van Der Schaft, C. S. Chen, F. P. T. Baaijens, C. V. C. Bouten, *Integr. Biol.* **2014**, *6*, 422.
[63] C. Fink, S. Ergün, D. Kralisch, U. Remmers, J. Weil, T. Eschenhagen, *FASEB J.* **2000**, *14*, 669.
[64] H. K. Voges, S. R. Foster, L. Reynolds, B. L. Parker, L. Devilée, G. A. Quaife-Ryan, P. R. J. Fortuna, E. Mathieson, R. Fitzsimmons, M. Lor, C. Batho, J. Reid, M. Pocock, C. E. Friedman, D. Mizikovsky, M. Francois, N. J. Palpant, E. J. Needham, M. Peralta, G. del Monte-Nieto, L. K. Jones, I. M. Smyth, N. R. Mehdiabadi, F. Bolk, V. Janbandhu, E. Yao, R. P. Harvey, J. J. H. Chong, D. A. Elliott, E. G. Stanley, et al., *Cell Rep.* **2023**, *42*, 112322.
[65] L. Goers, P. Freemont, K. M. Polizzi, *J. R. Soc. Interface* **2014**, *11*, 20140065.
[66] M. A. M. Vis, K. Ito, S. Hofmann, *Front. Bioeng. Biotechnol.* **2020**, *8*, 911.
[67] B. Abecasis, P. Gomes-Alves, S. Rosa, P. J. Gouveia, L. Ferreira, M. Serra, P. M. Alves, *Biotechnol. Bioeng.* **2019**, *116*, 1245.
[68] A. Kahn-Krell, D. Pretorius, B. Guragain, X. Lou, Y. Wei, J. Zhang, A. Qiao, Y. Nakada, T. J. Kamp, L. Ye, *New J. Bot.* **2022**, *10*, 1.
[69] M. Koivisto, T. A. Tolvanen, T. Toimela, I. Miinalainen, A. Kiviaho, J. Kesseli, M. Nykter, L. Eklund, T. Heinonen, *Sci. Rep.* **2022**, *12*, 13459.
[70] P. W. Burridge, S. A. Metzler, K. H. Nakayama, O. J. Abilez, C. S. Simmons, M. A. Bruce, Y. Matsuura, P. Kim, J. C. Wu, M. Butte, *Am. J. Transl. Res.* **2014**, *6*, 724.
[71] S. M. Ravenscroft, A. Pointon, A. W. Williams, M. J. Cross, J. E. Sidaway, *Toxicol. Sci.* **2016**, *152*, 99.
[72] E. Giacomelli, M. Bellin, L. Sala, B. J. van Meer, L. G. J. Tertoolen, V. V. Orlova, C. L. Mummery, *Development* **2017**, *144*, 143438.
[73] N. L. Tulloch, V. Muskheli, M. V. Razumova, F. S. Korte, M. Regnier, K. D. Hauch, L. Pabon, H. Reinecke, C. E. Murry, *Circ. Res.* **2011**, *109*, 47.
[74] H. Masumoto, T. Nakane, J. P. Tinney, F. Yuan, F. Ye, W. J. Kowalski, K. Minakata, R. Sakata, J. K. Yamashita, B. B. Keller, *Nat. Publ. Gr.* **2016**, *6*, 29933.
[75] V. D. Trikalitis, N. J. J. Kroese, M. Kaya, C. Cofiño-Fabres, S. ten Den, I. S. M. Khalil, S. Misra, B. F. J. M. Koopman, R. Passier, V. Schwach, *Biofabrication* **2023**, *15*, 015014.
[76] C. O. Lizama, A. C. Zovein, *Exp. Cell Res.* **2013**, *319*, 1247.
[77] D. Tirziu, F. J. Giordano, M. Simons, *Circulation* **2010**, *122*, 928.
[78] L. González-Mariscal, P. Nava, S. Hernández, *J. Membr. Biol.* **2005**, *207*, 55.
[79] J. R. Neely, M. J. Rovetto, J. F. Oram, *Prog Cardiovasc Dis* **1972**, *15*, 289.
[80] S. Mysling, K. K. Kristensen, M. Larsson, A. P. Beigneux, H. Gårdsvoll, L. G. Fong, A. Bensadouen, T. J. Jørgensen, S. G. Young, M. Ploug, *Elife* **2016**, *5*, 12095.
[81] A. Stoehr, M. N. Hirt, A. Hansen, M. Seiffert, L. Conradi, J. Uebeler, F. P. Limbourg, T. Eschenhagen, *Tissue Eng., Part A* **2016**, *22*, 326.
[82] V. Schwach, A. O. Verkerk, M. Mol, J. J. Monshouwer-Kloots, H. D. Devalla, V. V. Orlova, K. Anastassiadis, C. L. Mummery, R. P. Davis, R. Passier, *Stem Cell Rep.* **2017**, *9*, 1765.
[83] M. C. Ribeiro, R. H. Slaats, V. Schwach, J. M. Rivera-Arbelaez, L. G. J. Tertoolen, B. J. van Meer, R. Molenaar, C. L. Mummery, M. M. A. E. Claessens, R. Passier, *J. Mol. Cell. Cardiol.* **2020**, *141*, 54.
[84] E. S. Ng, R. Davis, E. G. Stanley, A. G. Elefanty, *Nat. Protoc.* **2008**, *3*, 768.
[85] A. D. Witty, A. Mihic, R. Y. Tam, S. A. Fisher, A. Mikryukov, M. S. Shoichet, R.-K. Li, S. J. Kattman, G. Keller, *Nat. Biotechnol.* **2014**, *32*, 1026.
[86] PromoCell GmbH, "Instruction manual fibroblasts", can be found under https://promocell.com/wp-content/uploads/product-information/manual/C-12375.pdf, **2024**.
[87] G. W. Serrao, I. C. Turnbull, D. Ancukiewicz, D. E. Kim, E. Kao, T. J. Cashman, L. Hadri, R. J. Hajjar, K. D. Costa, *Tissue Eng., Part A* **2012**, *18*, 1322.